Monthly Notices
of the
ROYAL ASTRONOMICAL SOCIETY

MNRAS **451,** 3815–3835 (2015) doi:10.1093/mnras/stv1191

H-ATLAS/GAMA and HeViCS – dusty early-type galaxies in different environments

N. K. Agius,[1] S. di Serego Alighieri,[2] S. Viaene,[3] M. Baes,[3] A. E. Sansom,[1⋆] N. Bourne,[4] J. Bland-Hawthorn,[5] S. Brough,[6] T. A. Davis,[7] I. De Looze,[3,8] S. P. Driver,[9,10] L. Dunne,[11,4] S. Dye,[12] S. A. Eales,[13] T. M. Hughes,[3] R. J. Ivison,[7,4] L. S. Kelvin,[9,10,14] S. Maddox,[12] S. Mahajan,[15] C. Pappalardo,[16] A. S. G. Robotham,[9,10] K. Rowlands,[10] P. Temi[17] and E. Valiante[13]

[1]*Jeremiah Horrocks Institute, University of Central Lancashire, Preston, PR1 2HE Lancashire, UK*
[2]*INAF - Osservatorio Astrofisico di Arcetri, I-50125 Firenze, Italy*
[3]*Sterrunkundig Observatorium UGent, Krijgslaan 281 S9, B-9000 Gent, Belgium*
[4]*Institute for Astronomy, University of Edinburgh, Royal Observatory, Blackford Hill, Edinburgh EH9 3HJ, UK*
[5]*Sydney Institute for Astronomy, School of Physics A28, University of Sydney, NSW 2006, Australia*
[6]*Australian Astronomical Observatory, PO Box 915, North Ryde, NSW 1670, Australia*
[7]*European Southern Observatory, Karl-Schwarzschild-Str. 2, D-85748 Garching, Germany*
[8]*Institute of Astronomy, University of Cambridge, Madingley Road, Cambridge CB3 0HA, UK*
[9]*International Centre for Radio Astronomy Research, The University of Western Australia, 35 Stirling Highway, Crawley, WA 6009, Australia*
[10]*School of Physics and Astronomy, University of St Andrews, North Haugh, St Andrews, Fife KY16 9SS, UK*
[11]*Department of Physics and Astronomy, University of Canterbury, Private Bag 4800, Christchurch 8140, New Zealand*
[12]*School of Physics and Astronomy, University of Nottingham, Nottingham NG7 2RD, UK*
[13]*School of Physics and Astronomy, Cardiff University, The Parade, Cardiff CF24 3AA, UK*
[14]*Institut fur Astro- und Teilchenphysik, Universitat Innsbruck, Technikerstrae 25, 6020 Innsbruck, Austria*
[15]*School of Mathematics and Physics, University of Queensland, Brisbane, QLD 4072, Australia*
[16]*CAAUL, Observatorio Astronomico de Lisboa, Universidade de Lisboa, Tapada de Ajuda, P-1349-018 Lisboa, Portugal*
[17]*Astrophysics Branch, NASA/Ames Research Center, MS 245-6, Moffett Field, CA 94035, USA*

Accepted 2015 May 22. Received 2015 April 30; in original form 2015 January 26

ABSTRACT

The *Herschel Space Observatory* has had a tremendous impact on the study of extragalactic dust. Specifically, early-type galaxies (ETG) have been the focus of several studies. In this paper, we combine results from two *Herschel* studies – a Virgo cluster study Herschel Virgo Cluster Survey (HeViCS) and a broader, low-redshift Herschel-Astrophysical Terahertz Large Area Survey (H-ATLAS)/Galaxy and Mass Assembly (GAMA) study – and contrast the dust and associated properties for similar mass galaxies. This comparison is motivated by differences in results exhibited between multiple *Herschel* studies of ETG. A comparison between consistent modified blackbody derived dust mass is carried out, revealing strong differences between the two samples in both dust mass and dust-to-stellar mass ratio. In particular, the HeViCS sample lacks massive ETG with as high a specific dust content as found in H-ATLAS. This is most likely connected with the difference in environment for the two samples. We calculate nearest neighbour environment densities in a consistent way, showing that H-ATLAS ETG occupy sparser regions of the local Universe, whereas HeViCS ETG occupy dense regions. This is also true for ETG that are not *Herschel*-detected but are in the Virgo and GAMA parent samples. Spectral energy distributions are fit to the panchromatic data. From these, we find that in H-ATLAS the specific star formation rate anticorrelates with stellar mass and reaches values as high as in our Galaxy. On the other hand HeViCS ETG appear to have little star formation. Based on the trends found here, H-ATLAS ETG are thought to have more extended star formation histories and a younger stellar population than HeViCS ETG.

Key words: methods: statistical – galaxies: elliptical and lenticular, cD – galaxies: evolution – submillimetre: galaxies.

⋆E-mail: aesansom@uclan.ac.uk

1 INTRODUCTION

Dust is a fundamental component of the interstellar medium (ISM) of galaxies for the thermodynamics and chemistry of the gas, for the dynamics of the accretion in dense star-forming clouds, and for the attenuation of UV/blue radiation and its re-emission in the far-infrared (FIR; Draine 2003). The relative amount of dust varies strongly with galaxy type, increasing by about three orders of magnitude on average along the Hubble sequence (e.g. Cortese et al. 2012a). The connection between dust and chemical evolution also varies with galaxy type. In late-type galaxies (LTG) dust is strongly linked with star formation (SF), both because it serves as a catalyst for the formation of molecular gas necessary for SF and because, being heated mostly by young stars, its emission traces the regions of SF. The same paradigm does not necessarily apply to early-type galaxies (ETG; comprising of ellipticals and lenticulars), where dust can be heated by the radiation field produced by evolved stars and can be more diffuse, therefore not serving as an SF catalyst. In addition, ETG, particularly those in clusters, can have much larger amounts of hot gas than LTG, not favouring the presence of dust.

It is therefore important to study dust in ETG separately from LTG and the *Herschel Space Observatory* (Pilbratt et al. 2010) has allowed several such detailed studies (Rowlands et al. 2012; Smith et al. 2012; di Serego Alighieri et al. 2013, hereafter S13, and Agius et al. 2013, hereafter A13). In particular, S13 searched for dust in a large optical sample of 910 ETG in the Virgo cluster, extending also to dwarf ETG, using the PACS (Poglitsch et al. 2010) and SPIRE (Griffin et al. 2010) instruments, and found it in 17 per cent of the elliptical galaxies, in 40 per cent of lenticulars (S0 + S0a) and in about 3 per cent of the dwarfs (dE + dS0). They showed that the presence of dust does not correlate with the presence of neutral gas (H I) and the dusty ETG do not appear to have bluer B–H colours, i.e. to be more star-forming than the non-dusty ones. On the other hand, A13 searched for dust, also with PACS and SPIRE, in a sample of 771 brighter ETG ($M_r < -17.4$ mag) over a very large volume (144 deg^2 and $0.013 \leq z \leq 0.06$) and found it in 20 per cent of the ellipticals and in 38 per cent of the lenticulars. Not only are these detection rates high, but also the relative amount of dust is higher than in Herschel Virgo Cluster Survey (HeViCS) and the dusty ETG have bluer colours, suggesting that they may be forming more stars. Furthermore, S13 found a dependence of the dust temperature on the stellar mass and on the average *B*-band surface brightness within the effective radius, but A13 did not.

These differences may be an effect of the environment, since Herschel-Astrophysical Terahertz Large Area Survey (H-ATLAS) covers a wide range of environments, potentially hosting extreme mergers or interactions, whilst HeViCS is limited to a cluster environment, which may be less favourable for dust. Bourne et al. (2012) pointed out that environment was a possible influence on the relatively low dust masses in Virgo cluster ETG, in comparison with their results for stacked red sequence galaxies from the Galaxy and Mass Assembly (GAMA) survey. Alternatively, the dusty H-ATLAS ETG could represent younger versions of the 'standard' ETG; i.e. they may have formed recently, or have more extended star formation histories (SFHs). In fact, if galaxy evolution is influenced by the environment, ETG in sparse environments are more likely to be at an earlier stage in their evolution than ETG in dense environments (e.g. Thomas et al. 2005). Some differences may also be explained by the different models used to estimate the dust mass or by limitations in the models or wavebands used. Although a single modified blackbody (modBB) fitting approach gives a good estimate of the mass of cold, diffuse dust grains in the ISM of galaxies at all redshifts (Dunne et al. 2000; Blain, Barnard & Chapman 2003; Pope et al. 2006; Dye et al. 2010; Bianchi 2013), it may not account for the emission from dust in warmer media, such as the grains surrounding birth clouds of hot, young stars, or colder dust that needs multiple temperature models. The addition of further modBBs allowing for different temperatures have been shown to improve such fits (Dunne & Eales 2001; Galametz et al. 2011; Dale et al. 2012). Furthermore, given the wealth of panchromatic data for HeViCS and H-ATLAS/GAMA ETG, it is possible to exploit multiwavelength spectral energy distribution (SED) fits which consider stellar emission at UV/optical wavelengths, the attenuation by dust and resultant emission in the infrared.

Temi et al. (2009a,b) and Amblard et al. (2014) have further investigated the diversity of ETG by studying the physical properties of a sample of local E and S0 galaxies. They find that many local S0 galaxies are quite distinct from ellipticals, containing dust and cold gas in amounts that may be sufficient to generate appreciable SF at rates as large as several $M_\odot$/yr. However in this paper, we cannot investigate in detail the differences between E and S0 galaxies, since they are difficult to distinguish in the H-ATLAS/GAMA sample because of their distance and the limited spatial resolution of Sloan Digital Sky Survey (SDSS) images.

In this paper, we compare the properties of the dust in ETG from both the HeViCS sample of S13 and the H-ATLAS/GAMA sample of A13, by characterizing them in a uniform way and taking into account data at shorter wavelengths, in an attempt to understand the differences and the reasons causing them.

This paper is laid out in the following manner. In Section 2, we describe the data available for the HeViCS and the H-ATLAS/GAMA ETG samples. In Section 3, we compare the two samples, while in Section 4 we discuss effects of environment. Panchromatic fits to the ETG SED are described in Section 5 and a discussion of derived parameters is given in Section 6, and is followed by our conclusions in Section 7. The photometric data obtained from *Wide-field Infrared Survey Explorer* (*WISE*) are described in Appendix A. We assume a flat Universe with $\Omega_M = 0.3$, $\Omega_\Lambda = 0.7$ and $H_o = 70\,\mathrm{km\,^{-1}s^{-1}}$ Mpc.

2 DATA

This section summarizes the different surveys utilized in constructing the ETG samples that will be compared in this work.

2.1 FIR surveys

The H-ATLAS[1] is the widest open-time extragalactic survey with the *Herschel Space Observatory*, with one of its ultimate science aims being the investigation of the dust content of the nearby Universe at $z<0.5$ (Eales et al. 2010; Dunne et al. 2011). This survey samples over ∼570 deg^2 of sky, covering a range of environments in a uniform way. Their data collection process involved parallel imaging with Herschel's two photometers, PACS (100 and 160μm; Poglitsch et al. 2010) and SPIRE (250, 350 and 500μm; Griffin et al. 2010), with a 60arcsec s^{-1} scan rate. H-ATLAS has a 5σ sensitivity limit of 33.5 mJy beam^{-1} at 250μm (Rigby et al. 2011) – this corresponds to a dust mass of $\sim 10^{5-7} M_\odot$ for a range of temperatures (15–30 K) at low redshift ($z \leq 0.06$).

H-ATLAS catalogues were constructed from maps as described in Pascale et al. (2011) and Ibar et al. (2010). Source extraction was based on emission greater than 5σ in any of the 3 SPIRE

[1] http://www.h-atlas.org

wavebands, described in detail for the Science Demonstration Phase in Rigby et al. (2011). Smith et al. (2011) gives a description of the likelihood-ratio analysis performed to identify *r*-band optical counterparts to the SPIRE submm selected sources. Based on the resultant positional and photometric information for the individual sources, PACS flux densities are measured using circular apertures placed at the SPIRE positions. Details of the Phase 1 H-ATLAS and the GAMA catalogues used in this paper can be found in A13.

The HeViCS[2] (Davies et al. 2010, 2012) is an audit of a large fraction (84 deg^2) of the Virgo Cluster in the same five Herschel bands as the H-ATLAS survey. This specifically samples the dense environment of a nearby cluster, going down to fainter luminosities than H-ATLAS. Additionally their observations are deeper than the H-ATLAS observations, with four linked cross-scans for HeViCS compared to a single cross-scan for H-ATLAS. HeViCS observations were performed in fast-parallel mode with PACS and SPIRE, with a scan rate of 60 arcsec s^{-1}. The HeViCS 5σ sensitivity at 250μm is 25–33 mJy for sources smaller than the point spread function (PSF; Auld et al. 2013; S13); depending on the dust temperature this corresponds to a dust mass of $\sim$0.2–1$\times10^5$M$_\odot$ at the 17 Mpc distance of the main Virgo cluster cloud. A detailed account of the data collection, reduction and flux measurements can be found in Auld et al. (2013) and in S13.

2.2 Multiwaveband data

The GAMA[3] is a spectroscopic and photometric survey dedicated to constructing a galactic data base which spans the electromagnetic spectrum from ultraviolet to radio wavebands (Driver et al. 2011). This campaign is being supplemented by imaging from surveys such as the SDSS in the optical (Abazajian et al. 2009), *GALEX* in the UV (Bianchi & GALEX Team 1999), UKIDSS-LAS in the NIR (Lawrence et al. 2007) and H-ATLAS (Eales et al. 2010) in the FIR/submm; all these surveys have overlapping data within the same regions and the photometry has been made self-consistent using an aperture matching technique described in Hill et al. (2011).

The spectroscopic element of GAMA has just been completed at the Anglo-Australian Telescope (AAT), with the most recent Data Release (DR2) from GAMA giving access to 70 000 new redshifts in the GAMA I regions (Hopkins et al. 2013; Liske et al., in preparation). These are three regions of 48 deg^2 each, centred at 9, 12 and 14.5 h (G09, G12 and G15) on the celestial equator. Spectroscopic completeness limits are given as apparent petrosian magnitude r$_{\rm pet}$ <19.4 mag in the G09 and G15 fields, and r$_{\rm pet}$ <19.8 mag in G12 for GAMA I.

The H-ATLAS equatorial fields coincide with those of GAMA, and matching between the two sets of data revealed $\sim$10 000 counterparts, using the likelihood ratio method (Bourne et al., in preparation). It is from within these counterparts that the H-ATLAS ETG sample is constructed, as described in A13 and Section 3.1. Section 2 of A13 gives details of the GAMA I data bases used in this current paper.

A very large set of data is available for galaxies in the Virgo cluster. In this nearby cluster, we can obtain accurate galaxy morphological classifications and observe galaxies covering a wide range of luminosities. The main original source of information is the Virgo Cluster Catalogue (VCC, Binggeli, Sandage & Tammann 1985; Binggeli, Popescu & Tammann 1993) which, together with Virgo SDSS data (Davies et al. 2014), remains the most complete optical catalogue, until the catalogue of the Next Generation Virgo Cluster Survey (NGVS; Ferrarese et al. 2012) becomes publicly available. The VCC is complete to photographic magnitude m$_{\rm pg}$ = 18.0, but also contains fainter galaxies. GOLDMine (Gavazzi et al. 2003) provides a compilation of data on VCC galaxies. Useful additions are the *GALEX* Ultraviolet Virgo Cluster Survey papers (GUViCS; Boselli et al. 2011; Boselli 2012) and the H I survey for ETG of di Serego Alighieri et al. (2007).

3 OVERVIEW OF ETG SAMPLES

This section compares and contrasts two ETG samples, which are described below. Particular emphasis is placed on the differences between the classification criteria for these samples. A summary of the results from their parent papers is also given.

3.1 H-ATLAS sample

From the sample of 771 ETG with $M_r \leq -17.4$ in the GAMA equatorial fields, the H-ATLAS detections comprise 220 Es and S0s with 5σ 250 μm from *Herschel*. Thus there are 551 ETG in our GAMA sample that are below this detection limit (the undetected H-ATLAS ETG). The optical counterparts in GAMA have reliability of association >0.8. The morphological classification process for all these ETG is fully described in A13; briefly, it was based on visual classification of blue, green and red optical galaxy cutouts into six groupings of E, S0, SB0a, Sbc, SBbc and Sd galaxies (see Kelvin et al. 2014 for a full account of this process). The galaxies classified in this way are GAMA I galaxies within a redshift range of $0.013 \leq z \leq 0.06$ and complete to an absolute magnitude cutoff of $M_r \leq -17.4$ – these limits are therefore also applicable to the ETG sample. We note that this sample lacks the faintest ETG close to the $M_r = -17.4$ limit, probably because these are dominated by the PSF and therefore excluded since they cannot be reliably classified (see above). We will discuss the effects of this selection in Section 3.3.

The ETG sample was constructed from the H-ATLAS detected E and S0 (which include both S0, S0a and Sa galaxies) galaxies from within this classified set of galaxies, with additional criteria imposed to remove any potential spiral structure, edge-on discs, or small objects which may be barely resolved and thereby possibly misclassified. Galaxies with AGN and LINER signatures in the optical BPT diagram (Baldwin, Phillips & Terlevich 1981) were also removed, so as to only consider galaxies with an FIR/submm SED dominated by thermal dust emission. This resultant sample contains 73 Es and 147 S0s, a few examples of which are shown as *g*-band SDSS cutouts in Fig. 1. Please see A13 for details of comparisons of properties between Hubble types, for the H-ATLAS sample.

A13 showed that the H-ATLAS submm detected ETG sample had unusual characteristics in comparison to the undetected ETG. In particular, both optical and UV-optical colours were typically quite blue, indicating some ongoing SF in these systems (see also Rowlands et al. 2012). The galaxy light profiles showed more exponential (or less centrally concentrated) luminosity distributions, which might indicate some recent merging activity, or may be an effect of dust attenuation, or a faint disc. Finally, an investigation of nearest neighbour galaxy surface density revealed that these ETG inhabit sparser environments than the non-detected ETG.

ModBBs with emissivity spectral index $\beta = 2$ and 350 μm mass absorption coefficient $\kappa_{350} = 4.54$ cm^2 g^{-1} (Dunne et al. 2011) were

[2] http://wiki.arcetri.astro.it/bin/view/HeViCS/WebHome
[3] http://www.gama-survey.org

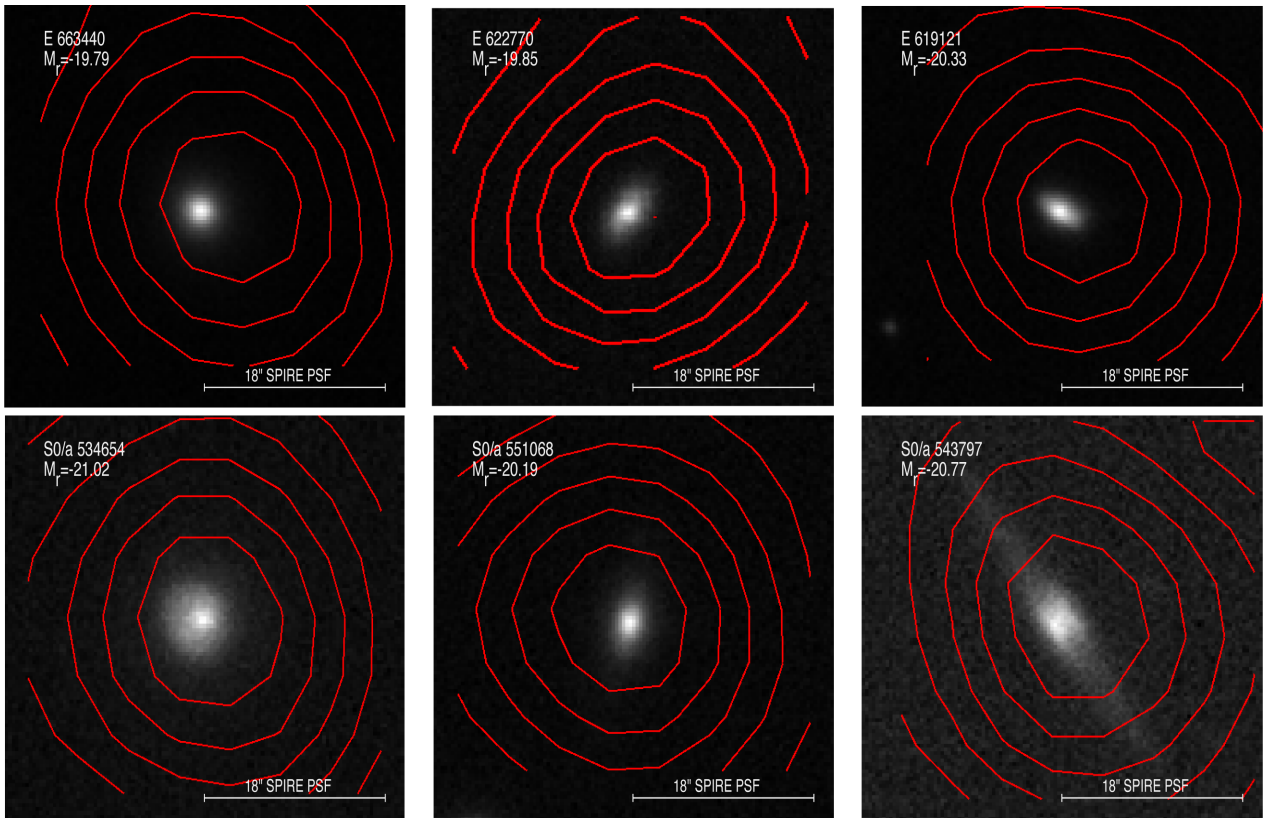

Figure 1. Example images of submm detected H-ATLAS galaxies with E (top) and S0 (bottom) classifications. The images are 40 arcsec by 40 arcsec SDSS *g*-band images with superimposed H-ATLAS 250 μm contours in red. These contour levels represent ∼15, 35, 55, 80 and 100 per cent of the 250 μm flux. Galaxy classification, catalogue ID and absolute *r*-band magnitudes are shown on the top-left of the images. The 18 arcsec SPIRE FWHM PSF, at 250 μm, is also shown in these images.

Table 1. Parameters indicating the types of ETG found in the submm detected H-ATLAS and HeViCS samples. Note that parameters for the HeViCS sample only include the 33 ETG with $M_r \leq -17.4$. The parameters shown include sample sizes, ranges of luminosity distances, stellar masses, *r*-band absolute magnitude, *r* and NUV band apparent magnitudes, total 250 μm fluxes and luminosities. Dust mass, dust-to-stellar mass ratio and environmental density ranges are also shown, calculated as described in the main text.

Parameter	H-ATLAS Det.		HeViCS Det.	
	min	*max*	*min*	*max*
Sample size (gals)	220		33	
Distance$_L$ (Mpc)	57.2	265.4	17.0	32.0
$\log_{10}(M_*)$ ($M_\odot$)	8.9	11.4	8.7	11.4
M_r (mag)	−18.2	−23.1	−17.4	−23.1
m_r (mag)	17.7	13.3	14.1	8.1
$m_{\rm NUV}$ (mag)	22.7	16.6	18.1	13.8
F_{250} (Jy)	0.033	0.770	0.013	7.992
L_{250} (W Hz^{-1})	1.6×10^{22}	4.3×10^{24}	4.4×10^{20}	2.8×10^{23}
$\log_{10}(M_{\rm d})$ ($M_\odot$)	5.91	8.54	4.48	6.67
$\log_{10}(M_{\rm d}/M_*)$	−4.44	−2.13	−6.29	−3.07
$\Sigma_{\rm gal}$ (gals Mpc^{-2})	0.001	37.08	29.19	463.10

fit to the PACS (100 and 160 μm) and SPIRE (250, 350 and 500 μm) data for 188 galaxies (see A13). These parameters are fixed to these values throughout this paper. A13 report a range of rest-frame dust temperature between 9 and 30 K and a range of dust masses between 8.1×10^5–3.5×10^8 $M_\odot$, with a mean dust-to-stellar mass ratio of $\log_{10}(M_{\rm d}/M_*) = -3.37$. These results are the key parameters which will be investigated within this paper, in comparison to the nearby ETG in the Virgo Cluster. A summary of the characteristics of H-ATLAS and HeViCS samples (described in Section 3.2) is given in Table 1.

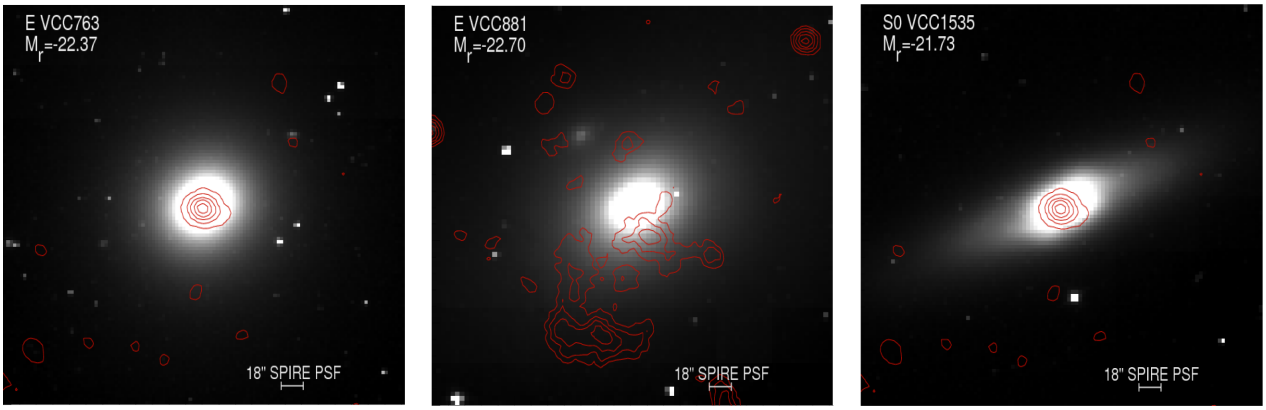

Figure 2. Example images of submm detected HeViCS galaxies with a variety of classifications. The images are 6 arcmin by 6 arcmin SDSS *g*-band images with superimposed HeViCS 250 μm contours in red. These contour levels represent the following percentages of the 250 μm flux: 14, 43, 71 and 100 per cent (VCC763), 18, 36, 55, 73 and 100 per cent (VCC881), 3, 28, 52, 76 and 100 per cent (VCC1535). Galaxy GOLDMine classification, identification and absolute *r*-band magnitudes are shown on the top-left of the images. Note that VCC 763 has a synchrotron component. The 18 arcsec SPIRE FWHM PSF is also shown in these images.

3.2 HeViCS sample

For HeViCS, S13 utilize an input optical sample from the VCC, constrained by ETG morphology (as compiled in GOLDMine; Gavazzi et al. 2003) but not limited in any other respect. Therefore their sample of 910 ETG spans a range of magnitudes, from dwarf systems to the most massive ETG, and contains classifications equal or earlier than S0a-S0/Sa types.

S13 found 52 ETG by searching for *Herschel* counterparts within one pixel (6 arcsec) and signal-to-noise (S/N) greater than 5, in the parent sample described above. The reliability of these counterparts is fully discussed in S13. In order to make a fair comparison with the brighter galaxies in the GAMA/H-ATLAS sample, we selected a bright subsample of the 910 ETG of the input HeViCS sample, by applying a cutoff of SDSS $M_r \leq -17.4$, as with the GAMA galaxies. This subsample is complete for the Virgo Cluster and contains 123 ETG. Out of these, 33 ETG are detected at 250 μm: their properties are given and contrasted to the H-ATLAS sample in Table 1. 16 of the 19 ETG detected at 250 μm, which have been removed, have formal GOLDMine dwarf classifications. From here on, these 33 ETG will form the HeViCS detected sample. Correspondingly 90 Virgo ETG with $M_r \leq -17.4$ are undetected at 250 μm. The magnitude cutoff $M_r \leq -17.4$ also has the effect of removing all those ETG identified as possible contaminating background sources in S13. Therefore all the 33 HeViCS ETG considered here have secure identifications. Fig. 2 shows a few examples of Virgo ETG detected in HeViCS. VCC763 and VCC1535 are shown to have centrally distributed submm emission, but VCC881 is a special case, as the submm contours are quite offset from the galactic centre. This is likely due to the streams linked with this galaxy, indicative of dwarf companion stripping (e.g. Trinchieri & di Serego Alighieri 1991; Kenney et al. 2008; Janowiecki et al. 2010).

Apparent *r*-band magnitudes for this ETG sample have been obtained from the work by Cortese et al. (2012b), where they calculated UV and optical asymptotic magnitudes for the Herschel Reference Survey (HRS) galaxies, some of which are in the Virgo cluster. This provided AB *r*-band magnitudes for 148 HeViCS galaxies; the remaining HeViCS galaxies have magnitudes calculated from the combination of *B*-band magnitudes from GOLDMine and the average $(B - r) = 1.02 \pm 0.26$ colour obtained from these 148 galaxies. These apparent magnitudes are then converted to absolute magnitudes using the GOLDMine distances and the appropriate galactic absorption.

Stellar masses were estimated for these galaxies using the method of Zibetti, Charlot & Rix (2009) whereby optical (and NIR when available) photometry and synthetic libraries are compared. Dust temperatures and masses were derived from modBB fits to the FIR/submm data. For the 33 massive (i.e. non-dwarf) ETG and the same values for β and κ_{350} as the H-ATLAS sample, dust temperatures and masses are given as 14.6–30.9 K and 3.0×10^4–4.7×10^6 $M_\odot$. Their mean dust-to-stellar mass ratio is $\log_{10}(M_d/M_*) = -3.93$.

3.3 Sample comparison

There are some clear differences between the two samples which need to be addressed before proceeding with a comparison of their properties. A primary concern is the difference in galaxy distance (see Table 1): HeViCS ETG are located in the nearby Universe at a distance between 17 and 32 Mpc, whereas H-ATLAS ETG are further away within a distance range of $56 \leq d_L \leq 269$ Mpc with an average distance of ∼195 Mpc. As a consequence, H-ATLAS ETG will have lower spatial resolution, larger luminosity at the optical detection threshold, and a higher dust-mass detection threshold. HeViCS ETG are very well resolved and have lower detection thresholds at all wavebands. For H-ATLAS, this results in the morphological classification not being as detailed as that completed for HeViCS. Therefore, H-ATLAS ETG can be identified as either E or S0 galaxies, but we cannot distinguish safely between these two classes, nor detect any dwarf galaxies, which in any case are excluded by the $M_r \leq -17.4$ limit. Also the completeness at this limit of H-ATLAS ETG is not as good as for the HeViCS ETG for the reasons explained in Section 3.1.

Given that this work will contain a statistical analysis of the properties of the two samples, it is important to consider whether the ETG sample sizes are statistically significant. Additionally, when comparing properties for the samples using statistical tests, it is preferable for the sample sizes to be of similar orders of magnitude in order to obtain a fair analysis. The H-ATLAS sample contains 220 ETG detected in the FIR whereas HeViCS contains 33 ETG (within the H-ATLAS magnitude cutoff of $M_r \leq -17.4$). Both samples are

large enough to run a Kolmogorov–Smirnov (KS) test, which is sensitive to fairly small differences between modest sized samples, to check whether the populations are similar. The sample sizes themselves are different with the HeViCS sample only containing ∼15 per cent of the H-ATLAS numbers, but the differences are not so large that such a test would be invalid.

HeViCS dust masses and specific dust masses are lower than those of the H-ATLAS sample by approximately an order of magnitude, even though the morphologies of the galaxies are similar and the stellar mass ranges overlap. This is due to the fact that the closest H-ATLAS ETG (those at $z \sim 0.013$ or distance $d_L \sim 56$ Mpc) are more than three times further away from us than the main Virgo cloud at 17 Mpc, and on average the H-ATLAS ETG are still much further away (see Table 1). Therefore smaller quantities of dust (at least 10 times smaller) can be detected in HeViCS ETG than in H-ATLAS. These differences need to be taken into account to avoid possible biased conclusions about the properties of ETG as a class.

Dust appears to be much more concentrated than stars in Virgo ETG, and more luminous ETG have higher dust temperatures (Smith et al. 2012, S13). The dust mass does not correlate clearly with stellar mass, while the dust-to-stellar mass ratio anticorrelates with galaxy luminosity. The dusty ETG appear to prefer the densest regions of the Virgo cluster. Contrary to H-ATLAS/GAMA ETG, the HeViCS ETG detected at 250 μm are not bluer than the undetected HeViCS ETG (di Serego Alighieri 2013).

The significant difference in 250 μm luminosities between the two samples also needs to be considered, especially given the similarity in optical luminosity between the two samples. We calculate this parameter for all the ETG. H-ATLAS ETG have a range of luminosities from 1.6×10^{22}–4.3×10^{24} W Hz^{-1}, whereas HeViCS have a range from 4.4×10^{20}–2.76×10^{23} W Hz^{-1}. We define a threshold luminosity, defined by the H-ATLAS flux limit of 33.5 mJy and maximum distance ($z = 0.06 \rightleftharpoons d_L = 269$ Mpc), which equates to 2.77×10^{23} W Hz^{-1}. There are 52 ETG (24 per cent) within H-ATLAS with detections below this threshold luminosity; therefore there is some overlap in FIR luminosity between the two samples. It is possible that the difference in luminosities is a direct result of the much larger volume covered by H-ATLAS/GAMA, which gives a larger chance of seeing rarer objects.

4 EXPLORING ENVIRONMENTS

Galaxies in the HeViCS sample are, by design, located in the Virgo Cluster. Although the cluster is an overall dense environment, the density is not homogeneous and will vary with position throughout the cluster. Conversely, because the ETG in the H-ATLAS sample were taken from a wide area of sky over a volume of redshift, they most likely belong to a range of environments, thus reaching lower densities. Therefore, a quantitative comparison of the environments inhabited by the ETG in both samples requires some form of estimation of the environmental density performed in a consistent manner.

4.1 Nearest neighbour densities

To calculate environmental densities, we utilize nearest neighbour surface densities. This has already been done to some extent for the H-ATLAS sample (Brough et al. 2013, A13), although a bright magnitude limit of $M_r \leq -20$ was imposed that may not accurately sample the true densities of these ETG. Nearest neighbour densities are now calculated which do not incorporate so bright a magnitude limit.

Chris Beaumont's IDL library[4] is used to calculate a smoothed map of the coordinates of all the galaxies in the HeViCS and H-ATLAS sample regions, respectively, based on the method in Gutermuth et al. (2005). Although we are only interested in the environments of the submm detected ETG, it is necessary to perform this routine on the entire population of galaxies within these regions to accurately depict the true density; this is the density-defining population (DDP). For every galaxy, the algorithm calculates the distance D_N to the *Nth* closest object and thus the surface density

$$\Sigma_{\rm gal} = \frac{N}{\pi D_N^2}. \quad (1)$$

The value of N chosen for these calculations is five as this is a good compromise given the effects of survey edges. Additional calculations are then required to convert the units of the surface densities from objects per square degrees to objects per square Mpc. For the HeViCS galaxies, this is a straightforward conversion using the distance of the galaxy.

These calculations are not as simple for the H-ATLAS sample; because of the large redshift range of the galaxies, Brough et al. (2013) and A13 limited the DDP for each sample galaxy to a velocity cylinder ± 1000 km s^{-1} over which the surface density is calculated, so that the latter is not influenced by galaxies at large distances, which clearly cannot have any environmental effect. This is also repeated here. Once each DDP has been created, the procedure described above for the HeViCS densities can be run, and surface densities created.

An additional restriction for these calculations is the imposed magnitude limit on the galaxies used to create the DDP. The Virgo Cluster galaxies can be detected down to much fainter magnitude limits than the higher redshift galaxies, and therefore surface densities for the latter are likely to be underestimated because dwarf galaxies which are detected in the Virgo cluster cannot be detected at higher redshifts. To avoid this, we set a magnitude limit on the DDP of $M_r \leq -17.4$ for both samples. This is the faintest limit which still ensures completeness also on the H-ATLAS/GAMA sample at $0.013 < z < 0.06$.

We test the calculated surface densities by comparing them with those derived by Brough et al. (2013) and displayed in A13. Fig. 3 shows a direct comparison between the two parameters, with a mostly linear relation defined. There are some galaxies from A13 which have higher surface densities than those calculated here: these are upper limits calculated for these galaxies flagged as lying at the edge of the GAMA regions. More importantly, the surface densities calculated in this work are systematically higher than those in A13. This is as expected, as the fainter DDP magnitude limit will include more galaxies in the calculation, resulting in higher densities.

4.2 Sample environments

There are three key points to be investigated when comparing the environmental densities of ETG in the H-ATLAS sample with those from the HeViCS sample. First, how do the respective submm detected samples differ in environment and is there any overlap? Next this study is extended to all ETG in A13 compared to all ETG in S13. Finally, it is also of interest whether the submm detected versus non-detected ETG in these respective samples vary in environment between themselves and if so, what the sense of this variation is.

[4] http://www.ifa.hawaii.edu/users/beaumont/code/

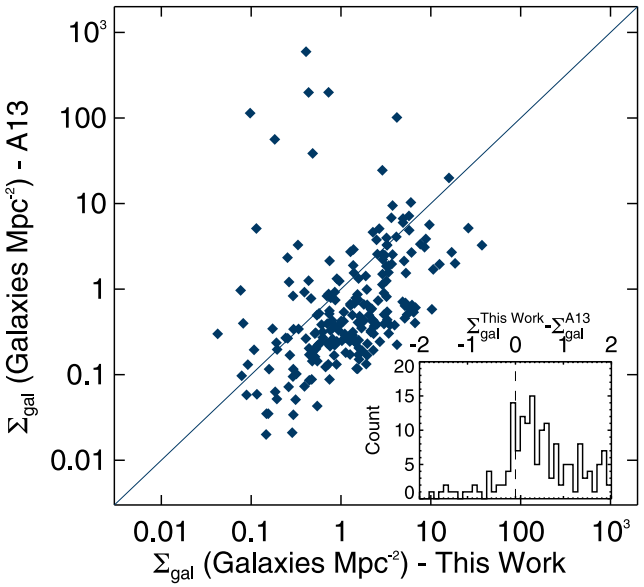

Figure 3. A comparison of the nearest neighbour densities for the H-ATLAS sample as calculated in this work with those calculated in A13. The key difference in the calculation of these densities is the magnitude limit of the DDPs required to calculate these values. A one-to-one correlation is shown to aid comparison. The inset plot shows the quantitative difference between the two in histogram form.

Trends of these distributions of densities are investigated in Figs 4 and 5. A KS test of the submm detected samples' densities in Fig. 4(a) reveals a probability of only 2×10^{-26} of the two distributions being drawn from the same parent distribution. H-ATLAS and HeViCS ETG clearly reside in very different environments, where HeViCS ETG are dominated by the dense cluster environment; the H-ATLAS ETG on the other hand mostly occupy sparse and non-cluster environments.

Examination of the samples including those ETG without submm detections in Fig. 4(b) reveals the probability of ETG residing in the same environments is also zero, yet there is a modest overlap in the environments for the two samples between $20 < \Sigma_{gal} < 100$ gals Mpc^{-2}. This overlap can mostly be associated with those ETG which are not detected at submm wavelengths and is explored further in Fig. 5. Note that such an overlap is not apparent in Fig. 4(a) for the submm detected samples. The GAMA survey as a whole is deep and wide enough to sample a broad range of galaxy environments, from isolated field galaxies, to pairs, and both small and large groups (e.g. Robotham et al. 2011). However, it does not sample well the densest regions of the Universe as found in large clusters, since these are very rare environments. This can be seen in Fig. 4(b), which shows that the GAMA galaxies in the three equatorial fields sampled in A13 do not extend up to the densities found in the Virgo cluster. Thus this ETG study is comparing and contrasting largely different environments.

Fig. 5 explores the trend of surface density between submm detected and undetected ETG for the respective samples. KS tests for both sets of distributions indicate that there is a significant difference between the H-ATLAS distributions (<1 per cent probability of them being the same), but that the HeViCS distributions are very similar. This indicates no environment density preference within the Virgo ETG (for the subsample of data used here). For H-ATLAS (Fig. 5a), the submm detected ETG have lower surface densities with respect to those of the undetected ETG – also shown in fig. 10 of A13. In Fig. 5(b) for the HeViCS sample, the opposite effect is suggested. This latter result was noticed by S13 (and contrasted with the result for H I detections and non-detections), when fainter galaxies were included. The tendency found in HeViCS for dusty ETG to occupy the densest regions is consistent with the higher dust detection rate found for HRS ETG inside the Virgo Cluster than for those outside, particularly for lenticulars (Smith et al. 2012).

This particular difference may be attributed to the fact that the two samples are environmentally very different (as explicitly shown in Fig. 4), with the H-ATLAS sample occupying sparse environments and the HeViCS sample occupying a high-density environment. However, given that both strangulation and ram pressure stripping in dense environments are known to typically remove the ISM from galaxies,[5] it is expected that submm detected galaxies would be in lower density regions than undetected galaxies. The fact that the Virgo ETG are not exhibiting this behaviour indicates some other processes governing the presence of dust within these systems. Attention could be drawn to the case of M86: a Virgo elliptical which appears to have acquired its ISM via the stripping of gas and dust from a nearby spiral (Gomez et al. 2010). Smith et al. (2012) also suggested that all their ETG acquired their dust through mergers. Conversely, based on the lack of evidence for externally acquired material, Davis et al. (2013) argue against accretion as a general mechanism for gaining gas and dust in Virgo ETG.

An additional effect which may be contributing to this difference is the ability of HeViCS to detect dust to lower levels than H-ATLAS: S13 amongst others found Virgo ETG with dust masses as low as 10^5 M$_\odot$, and these lower dust masses appear to be quite common in the Virgo Cluster. Therefore by definition the dusty Virgo ETG are different to those being found by H-ATLAS. We observe that in the Virgo cluster there are no ETG with a 250 μm luminosity above 2.77×10^{23} W Hz^{-1}, which is equivalent to the threshold luminosity of H-ATLAS at the redshift upper limit ($z = 0.06$). This is unexpected given that the samples are matched in optical luminosity ($M_r \leq -17.4$), however it does explain the differences in dust masses currently being observed. Therefore, this difference in environments may be a cause of the differences in dust levels in these ETG (dust is destroyed in denser environments).

Another possible cause for this difference that should be considered is the morphological classification of the ETG. HeViCS ETG have high enough optical resolution that they can be definitively categorized into their separate morphologies. Given that H-ATLAS ETG lie at higher redshifts, their associated classifications cannot be assigned the same level of accuracy as the HeViCS ETG and in fact, Kelvin et al. (2014) group S0 and Sa galaxies together in their classifications. Since specific dust ratio of galaxies systematically increases when moving from ETG to LTG (Cortese et al. 2012a; Smith et al. 2012), it is possible that a change in the threshold between ETG and late-type classification can skew the results. It is also well known that ETG prefer denser environments (e.g. Dressler 1980). Therefore any spurious LTG which may exist in the H-ATLAS sample are likely to have both high dust-to-stellar mass ratio and sparser environments, thereby skewing the sample in the direction being seen.

This last possibility can be investigated further by estimating possible contamination levels for the H-ATLAS sample. Original classifications from Kelvin et al. (2014) revealed 999 ETG, of which 285 were only agreed on by two of the three classifiers. Assuming

[5] For example, dust stripping has been observed to be ongoing in the Virgo Cluster (Cortese et al. 2010a,b).

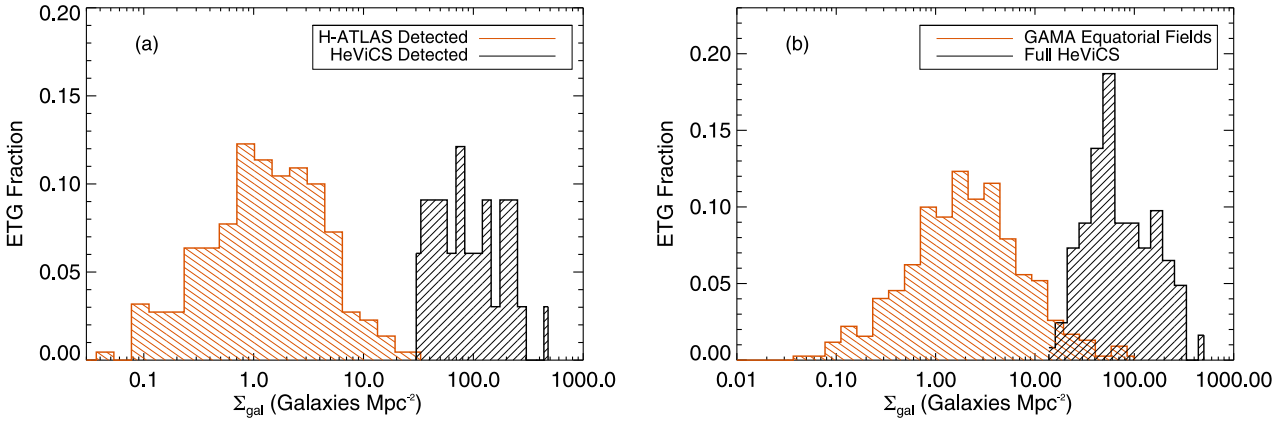

Figure 4. Left-hand panel: normalized distributions of submm detected ETG in H-ATLAS (orange histogram) and HeViCS (black histogram) samples. Right-hand panel: distributions of the combination of submm detected and undetected ETG in H-ATLAS (orange) and HeViCS (black).

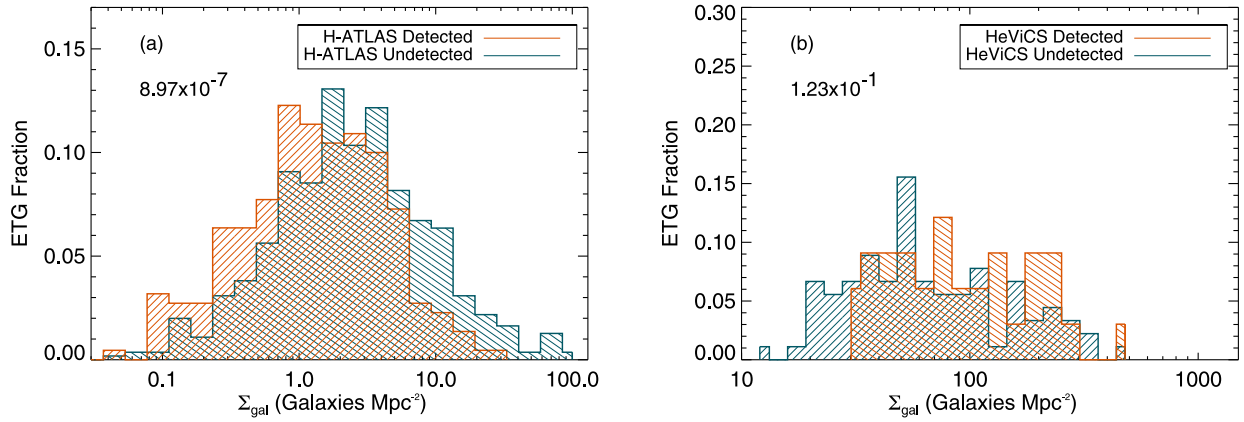

Figure 5. Left-hand panel: normalized distributions of submm detected (orange histogram) and submm undetected (blue histogram) ETG in H-ATLAS. Right-hand panel: distributions of submm detected (orange histogram) and submm undetected (blue histogram) ETG in HeViCS. KS probabilities for whether the presented samples are drawn from the same distribution are shown in the top left of the plots.

that each classifier has approximately equal weight, then these two-way agreements are estimated to be correct ∼two-thirds of the time, leaving ∼95 incorrect classifications (LTGs misclassified as ETGs). Additional criteria in A13 for creating the ETG samples included size and flattening (which removed 32 galaxies from the H-ATLAS sample, of which some may be LTG), plus evidence of spiral structure (which removed a further 22 galaxies from the H-ATLAS sample, which are all LTG). This reduces the potential number of contaminants to about 41 to 73 LTG. This is only ∼ 5–9 per cent of our sample of 771 ETG, whereas we detect 29 per cent of our ETG sample in the submm. Therefore, our observations are not consistent with resulting from LTG contamination alone. These values are estimates. This question of contamination of the H-ATLAS ETG sample will be better addressed in future through the use of deeper, sharper images from the VISTA and VST surveys covering GAMA areas (e.g. Sutherland et al. 2015).

5 MULTIWAVELENGTH SED FITS

The photometric data of both the HeViCS and H-ATLAS sample cover a wide wavelength range. Intrinsic information is encoded in the SED of each galaxy. Certain wavelengths are directly linked to a single component (e.g. NIR emission traces the old stellar population), while others are ambiguous (e.g. optical light is influenced by both stars and dust). It is therefore useful to treat the multiwavelength information of a galaxy at the same time using a complete model.

5.1 MAGPHYS

MAGPHYS – Multiwavelength Analysis of Galaxy Physical Properties (da Cunha, Charlot & Elbaz 2008) is a Bayesian fitting code which is able to model the UV to submm SED of galaxies. The program relies on a multicomponent galaxy model to predict the flux in each wavelength. Starting from an initial mass function (IMF) from Chabrier (2003), stellar components are evolved in time using the stellar population synthesis (SPS) model of Bruzual & Charlot (2003). The interaction of starlight with diffuse interstellar and star-forming region dust is calculated from the two-component Charlot & Fall (2000) extinction model. One of the key points of MAGPHYS is the physically realistic imposed energy balance between absorbed starlight and dust emission.

Emission from dust grains is modelled using a series of modBB functions and a fixed template for polycyclic aromatic hydrocarbon (PAH) features, as described in da Cunha et al. (2008). The free parameters in this dust model are the relative contributions of each component to the total IR emission and the temperatures of the warm circumstellar dust $T_{\rm W}^{\rm BC}$ and cold interstellar dust $T_{\rm C}^{\rm ISM}$. We adopt an expanded version of MAGPHYS (da Cunha, private communication) in the sense that the temperature ranges for warm and cold dust

are broadened to 30 K $< T_{\rm W}^{\rm BC} <$ 70 K and 10 K $< T_{\rm C}^{\rm ISM} <$ 30 K, respectively. This allows for a wider possible range of temperatures found in some systems. It results in longer computation times, but permits better sampling of cold and low star-forming environments.

A vast library is constructed by randomly drawing parameter sets from the above model and constructing template SEDs with these sets. The expanded version of MAGPHYS that we use here has 50 k optical and 75 k infrared templates in the library. For the dust an absorption coefficient of $\kappa_{350} = 4.54$ cm^{2}g^{-1}, with $\beta = 2$ is assumed. The observational SED is then modelled by comparing a library of stochastic models (as described in da Cunha et al. 2008) to the observed data and weighing the output parameters with the corresponding χ^2, constructing probability distribution functions (PDFs). Depending on the data coverage of the SED, some parameters are more accurately constrained than others. In this paper, we limit ourselves to the parameters listed below.

(i) Cold and warm dust are responsible for the large part of the total dust mass in galaxies ($M_C^{\rm ISM}$ and $M_W^{\rm ISM}$, respectively). Warm dust in birth clouds ($M_W^{\rm BC}$) can also contribute. The contributions of hot dust and PAHs are accounted for in a multiplicative factor of 1.1. Thus, the total dust mass is the sum of these components,

$$M_{\rm dust} = 1.1(M_W^{\rm BC} + M_W^{\rm ISM} + M_C^{\rm ISM}). \quad (2)$$

(ii) Cold dust in the diffuse ISM has an equilibrium temperature represented by $T_C^{\rm ISM}$.

(iii) Accordingly, the equilibrium temperature of warm dust in birth clouds is represented by $T_W^{\rm BC}$.

(iv) The total amount of infrared light emitted by dust grains is parametrized in the total dust luminosity $L_{\rm dust}$.

(v) The total stellar mass M_* as derived from the SPS models.

(vi) The star formation rate (SFR) is an average of the mass of stars formed per year, during the past 100 Myr. The underlying SF law is an exponentially declining SFR starting from the birth of the galaxy. Throughout the lifetime of the galaxy, there is a random chance of starbursts taking place.

(vii) The ratio of the SFR and M_* is then called the specific star formation rate (sSFR).

(viii) The time at which the galaxy is formed, $T_{\rm form}$, is defined as the age of the oldest stellar population.

(ix) The time at which the last starburst ended, $T_{\rm lastb}$.

5.2 Data coverage of the SED

Good coverage of the panchromatic SED is desirable to ensure reliable modelling. The GAMA/H-ATLAS data set comprises of self-consistent photometry based on a standard format. Therefore, the H-ATLAS ETG sample has the following data coverage of the SED: *GALEX* FUV and NUV, SDSS *ugriz*, UKIDSS *YJHK*, *WISE* *W*1–*W*4, PACS 100 and 160 μm and SPIRE 250, 350 and 500 μm. Note that some galaxies are missing data as detailed below:

GALEX FUV: 38 galaxies (17 per cent)
GALEX NUV: 36 galaxies (16 per cent)
WISE *W*1–*W*3: 5 galaxies (3 per cent)
WISE *W*4: 90 galaxies (41 per cent)
PACS 100 μm: 19 galaxies (9 per cent)
PACS 160 μm: 26 galaxies (12 per cent).

Missing galaxies in these wavebands are due to an inability to match the optical source to a counterpart in the specific waveband (i.e. no detection). The 22 μm *WISE* *W*4 band in particular suffers from a low detection rate due to the waveband's low S/N. Data in other wavebands is complete for all the galaxies.

In the case of the HeViCS ETG, the UV part of the spectrum is covered by fluxes from the *GALEX* catalogue except for the 12 galaxies which are also in HRS. For those, fluxes from Cortese et al. (2012a) were used. Optical and NIR filters include *UBV* & *JHK* from the GOLDMINE archive (Gavazzi et al. 2003).

WISE (Wright et al. 2010) detected almost all galaxies in the HeViCS sample during its all-sky survey. Unfortunately archival fluxes caused inconsistencies in the SED fits. The MIR is an ambiguous regime, with both emission from old stars and hot dust. Sufficient sampling and correct flux determination are vital to disentangle both components in an SED fit. We therefore chose to redo the flux measurements on the archival *WISE* images and minimize the contamination of foreground stars. Appendix A gives more detail on the measurements.

Herschel observations at 100–500 μm were taken from S13 and complete our data set.

5.3 SED results

MAGPHYS was used to fit energy balance models to each of the HeViCS and H-ATLAS ETG, as described above. Figs 6 and 7 show example MAGPHYS fits to one of the H-ATLAS and HeViCS ETG, respectively, with the resultant PDFs for a variety of fit parameters shown in the lower panels. MAGPHYS cannot include a synchrotron component and is therefore unable to correctly fit the four dusty HeViCS ETG with such a component, and therefore these are excluded from the multiwavelength analysis.

In order to gain some insight on the goodness-of-fit for each galaxy, the 29 (33 minus 4 synchrotron galaxies) HeViCS fits were visually inspected and assigned a flag for 'good' or 'poor' fit. Four galaxies were assigned 'poor fit' status – each of these fits had an associated reduced χ^2 value[6] greater than 4. This was then chosen as the criterion to assess whether the H-ATLAS fits were 'good' or 'poor'. 11 H-ATLAS systems were found to have 'poor fits' (PF). These 15 galaxies from the two samples are also highlighted in future plots to separate them from the rest of the sample. Additionally, all ETG with 'PF' or a synchrotron radio component are excluded in any further statistical analysis in this section.

5.3.1 *Contrasting derived parameters*

As described in Sections 3.1 and 3.2, A13 and S13 fit single modBBs to their FIR/submm data to obtain dust masses and temperatures for their ETG. These dust masses are used to evaluate the dust-to-stellar mass ratio which is plotted as a function of stellar mass in the left-hand panel of Fig. 8. The stellar masses are from A13 and S13. The effects of detection limits are illustrated. The red dashed lines in Fig. 8 represent the range of dust mass detection limits at the 250 micron flux limit of 33.5 mJy for the H-ATLAS sample, with the lower line for nearby ($z = 0.013$), high-temperature (30K) detection limits (as shown in A13) and the upper line for far ($z = 0.06$), low-temperature (15K) detection limits. This includes the typical temperature range of most H-ATLAS detections. Below the lower line no detections are expected and above the upper line all sources in this temperature and redshift range are detectable. Between the two lines detectability depends on the distance and dust temperature

[6] The MAGPHYS χ^2 is a constraint on the best-fitting theoretical template SED and hence the most likely fit.

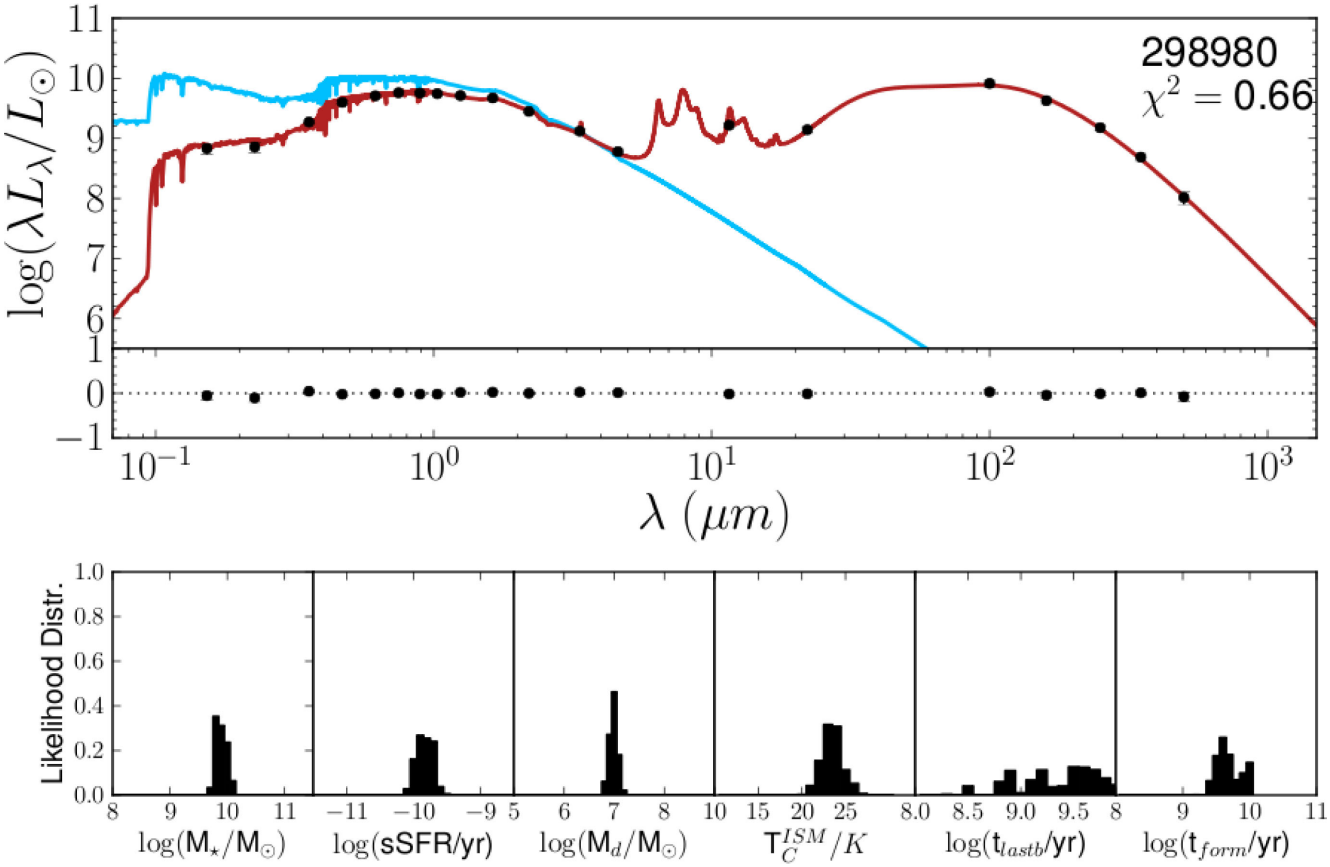

Figure 6. MAGPHYS rest-frame SED fit to H-ATLAS elliptical galaxy 298980. The SED is fit to observed photometry in the FUV, NUV, SDSS *ugriz*, UKIDSS *YJHK*, *WISE W*1, *W*2, *W*3 and *W*4, PACS 100, 160 μm and SPIRE 250, 350 and 500 μm wavebands (black points). The red line shows the overall attenuated model fit, whilst the blue line shows the unattenuated optical model. Below are the residuals from the fitted points, and below these are the likelihood probability functions for parameters of this elliptical galaxy.

of sources, with decreasing likelihood of detection going towards the lower line. The blue dot–dashed lines represent the corresponding limits for the HeViCS 250 micron flux limit of 25.4 mJy, the distance range of HeViCS sources (17–32 Mpc), and considering the effects of different dust temperatures for the various morphological types from Section 4.1 of S13. The specific dust mass detection limits are lower for the HeViCS sample, which is nearby, mostly at a distance of 17 Mpc. Fig. 8 shows a key difference in the normalized dust levels of the two ETG samples. It indicates that the HeViCS ETG have less dust, by a factor of 10 or more, than the H-ATLAS ETG. This difference is due to the much lower dust detection limit of HeViCS, whose galaxies are approximately 10 times closer than the H-ATLAS galaxies. However, it remains to be understood why there are no HeViCS ETG as dusty as the dusty H-ATLAS ETG, at fixed stellar mass.

A two sample KS test can be applied to the left plot in Fig. 8 by considering a diagonal line parallel to the limits and above which there are no HeViCS detections. This line goes through VCC1535 (at $\log_{10}(M_*) = 10.94$ and $\log_{10}(M_d/M_*) = -4.28$ in Fig. 8 left plot). 162 H-ATLAS/GAMA ETG lie above this line, out of 771 GAMA ETG with $M_r < -17.4$ mag. For the Virgo sample there are 123 (including all detected and undetected) ETG with $M_r < -17.4$ mag in the HeViCS area, which all lie somewhere below the diagonal line. Therefore the KS statistic is 0.21, which for these optical sample sizes has a probability <0.1 per cent of them being the same. Thus the two samples differ significantly from each other in Fig. 8. More studies of ETG in other clusters would help to verify if this is a difference due to environmental density.

Normalized dust mass calculated from MAGPHYS is shown plotted against stellar mass in the right-hand panel of Fig. 8, where the stellar masses are also from MAGPHYS. Both ModBB and MAGPHYS plots are shown side-by-side for ease of comparison. Qualitatively, there is little difference between these distributions. There is a negative trend found for this relationship for both these samples, partly driven by selection effects in the lower-left corner.

Dust properties from MAGPHYS fits are examined and contrasted to the modBB solutions in Figs 9(a) and (b). The MAGPHYS most likely[7] cold dust temperature and overall dust mass is shown on the *x*-axis, and modBB solutions are shown on the *y*-axis for both samples of ETG. As previously stated, PF are shown as different symbols to separate them from the GF.

Fig. 9(a) shows that dust temperatures are similar, except for a few outliers that vary more significantly between the fitting methods. These tend to be for galaxies without PACS detections. The scatter observed here is in the sense that MAGPHYS assigns higher temperatures to the likely cold dust grain distributions.

[7] The most likely value of a parameter is chosen as the median of the probability distribution functions output by MAGPHYS.

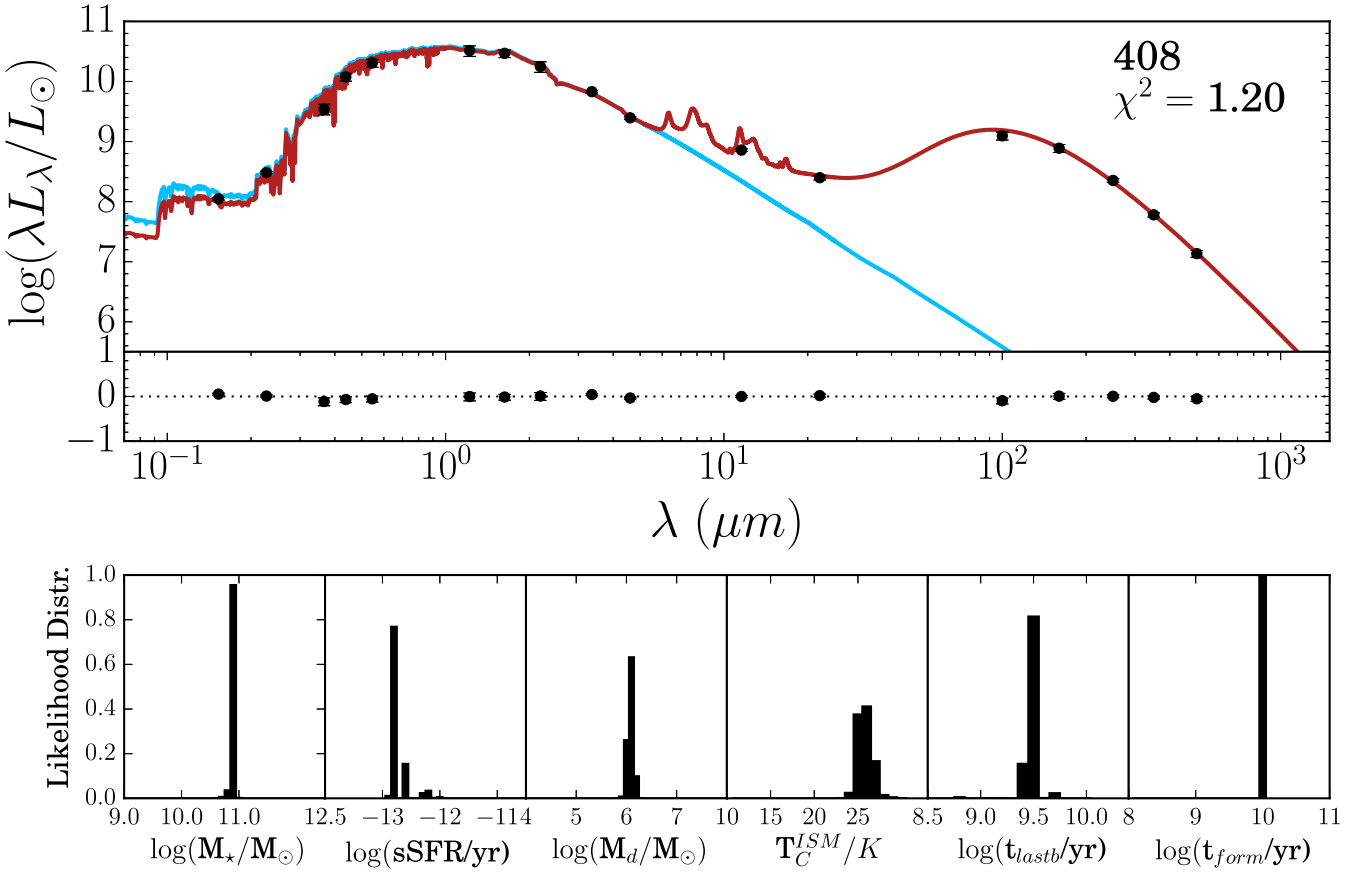

Figure 7. MAGPHYS rest-frame SED fit to HeViCS elliptical galaxy VCC 408. The SED is fit to observed photometry in the FUV, NUV, *UBV*, 2MASS *YJHK*, *WISE W*1, *W*2, *W*3 and *W*4, PACS 100, 160 μm and SPIRE 250, 350 and 500 μm wavebands (black points). The red line shows the overall attenuated model fit, whilst the blue line shows the unattenuated optical model. Below are the residuals from the fitted points, and below these are the likelihood probability functions for parameters of this elliptical galaxy.

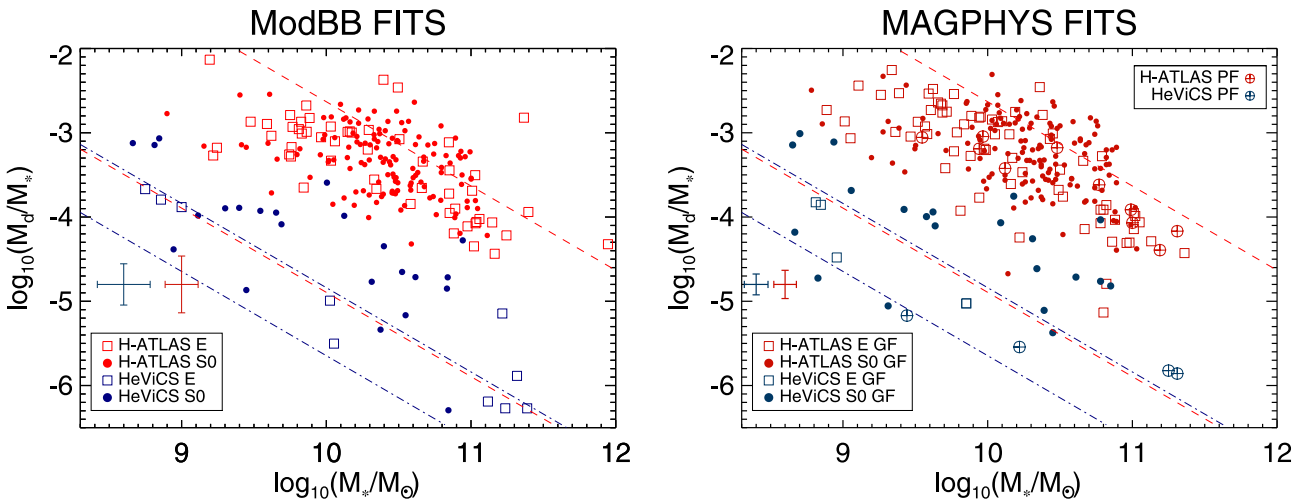

Figure 8. Dust-to-stellar mass ratio plotted as a function of stellar mass calculated using ModBBs (left-hand panel) and MAGPHYS (right-hand panel). HeViCS (blue points) and H-ATLAS (red points) samples are shown in both plots, and galaxies are subdivided into E (red squares for H-ATLAS and blue squares for HeViCS) and S0 (red dots for H-ATLAS and blue dots for HeViCS) classifications. In the MAGPHYS plot, galaxies with PF are encircled crosses in the samples' respective colours, while all other points are good fits (GF). Error bars in the left-hand panel give the mean overall uncertainty on the points from ModBB fits, in the same colours as their respective samples. In the left plot, diagonal lines represent the range of dust mass detection limits for the samples in their respective colours (see Section 5.3.1 for details). These same lines are included as a guide only in the right plot. Error bars in the right-hand panel give 1σ to each side of the PDF.

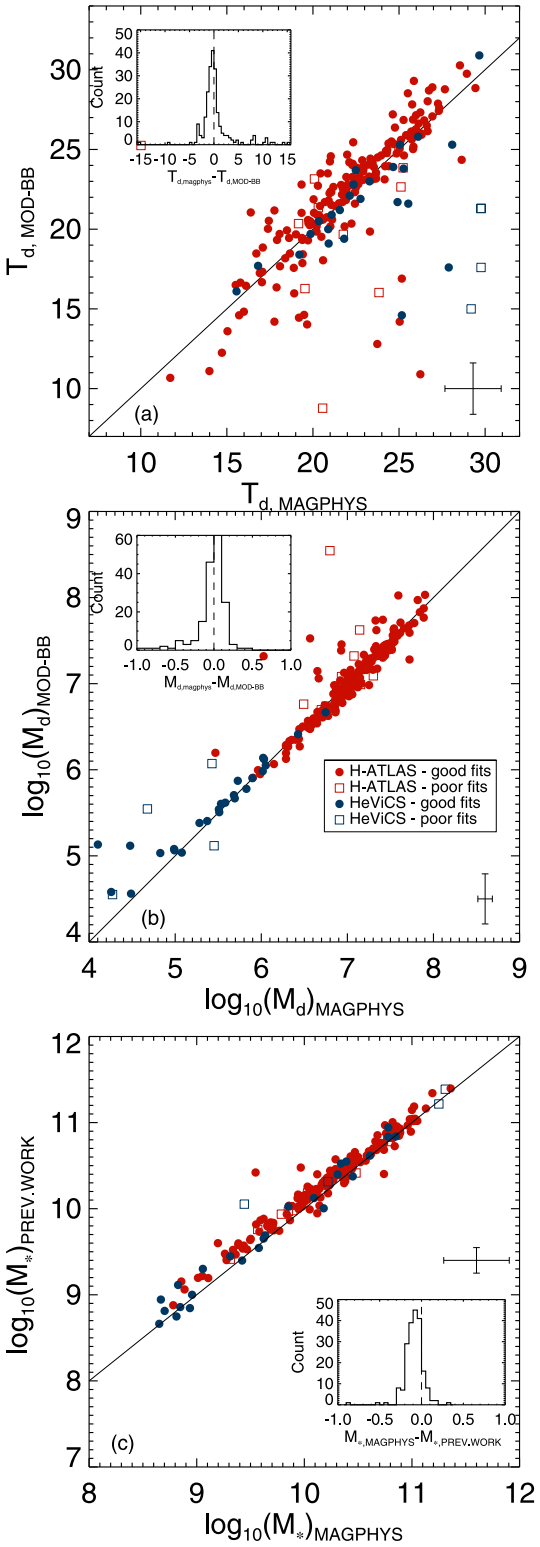

Figure 9. Comparison of derived cold dust temperature (top), dust mass (centre) and stellar mass (bottom), where the *y*-axis represents values from modBB fitting and the *x*-axis represents MAGPHYS fitting results. For the stellar mass comparison, the *y*-axis represents stellar mass values from A13 and S13. The H-ATLAS sample is plotted in red and HeViCS ETG are plotted in blue. Galaxies with PF ($\chi^2 \geq 4.0$) are shown as open squares. The solid line is a one-to-one line and error bars represent the mean 1σ errors in either direction for both samples. Inset plots show the difference offset from zero for each parameter.

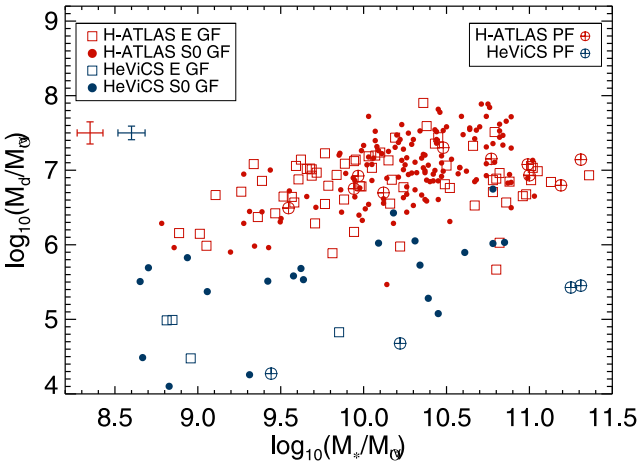

Figure 10. MAGHPYS dust mass plotted as a function of stellar mass. HeViCS (blue points) and H-ATLAS (red points) samples are shown, where galaxies are subdivided into E (red squares for H-ATLAS and blue squares for HeViCS) and S0 (red dots for H-ATLAS and blue dots for HeViCS) classifications. Galaxies with PF are encircled crosses in the samples' respective colours. Error bars give 1σ to each side of the PDF, in the same colours as their respective samples.

This difference may result from the fact that MAGPHYS fits multiple temperature components, unlike the single component ModBB. More MIR data coverage would help to constrain the dust temperatures in these outliers. However, these differences in temperatures do not necessarily cause similar scatter in other derived parameters.

MAGPHYS dust mass shows a better correspondence with dust masses derived from modBB fitting (see Fig. 9b). There is a slight offset for some galaxies in both samples from the $x = y$ plane – typically the modBB fitting appears to give higher dust masses. This is because MAGPHYS assumes a higher on average dust temperature than modBB fitting, thereby resulting in lower dust masses.

These tests reveal that the dust mass parameter is well described by both a modBB and MAGPHYS, as the mean results for the two samples do not change substantially, nor do the KS-test probabilities differ between the two methods. However, a small difference is found between the stellar masses derived by GAMA/HeViCS teams and those derived by MAGPHYS. Fig. 9(c) shows that stellar masses obtained with MAGPHYS are on average slightly smaller (by ∼0.1 dex) than those obtained previously, particularly at small masses. Taylor et al. (2011) showed that inclusion of UKIDSS fluxes slightly biases stellar mass measurements in this way. This is a small effect for the current applications. No systematic difference between HeViCS and H-ATLAS ETG is apparent in Fig. 9(c), which demonstrates that the previous stellar masses were also obtained consistently for the two samples.

We compare the relationship between derived dust and stellar mass for the two samples in Fig. 10. Trends are found for both H-ATLAS and HeViCS ETG, with correlation coefficients of $r_P = 0.42$ and 0.58, respectively, both with <1 per cent probability of chance occurrence. The difference in dust mass between the samples is highlighted by the ranges exhibited: $4.1 \leq \log(M_d/M_\odot) \leq 6.7$ for HeViCS and $5.5 \leq \log(M_d/M_\odot) \leq 7.9$ for H-ATLAS. Results from stacked data for red galaxies in (Bourne et al. 2012, their fig. 16) show a similar trend to that of the H-ATLAS ETG shown in Fig. 10. Following a similar KS test as previously, but using a line through the upper edge of the HeViCS detections in Fig. 10, we find 197 H-ATLAS detections above the line, out of 771 GAMA ETG. This gives a KS statistic of 0.25, which for these optical sample sizes

gives a probability <0.001 per cent of the Virgo ETG being drawn from the same parent population as the GAMA ETG. In other words, the *proportion* of dusty ETG is much higher in the GAMA sample than in the Virgo sample.

6 DISCUSSION

6.1 Mock catalogues and detection limits

We further test how the two samples of ETG compare in the left plot of Fig. 8 by carrying out Monte Carlo simulations for the Virgo galaxies, to account for the sample selection effects of the GAMA galaxies. 500 mock catalogues, each with 771 galaxies (as in the GAMA ETG sample), are generated by randomly sampling the Virgo ETG (for their dust mass, stellar mass and submm fluxes) and placing them at distances randomly selected from the GAMA ETG sample. The observed Virgo ETG submm fluxes (or non-detections) in 250 and 350 micron *Herschel* bands are then transformed to fluxes at the new distances, taking into account *K*-corrections (as in equation 2 of Dunne et al. 2011). Thus fluxes significantly decrease due to the larger distances and slightly increase due to *K*-corrections in the submm.

For each mock catalogue, the number of expected submm detections above the H-ATLAS limits (5σ at 250 μm and 3σ at 350 μm, as in A13) is calculated and expressed as a percentage of the 771 galaxies. The predicted mean and standard deviation is then 0.92 ± 0.36 per cent detections, with standard deviation calculated from the spread of results amongst the 500 mock catalogues. For GAMA ETG 188 out of 771 galaxies were actually detected (above those H-ATLAS limits, as in Fig. 8 left). This corresponds to 24.4 ± 2.0 per cent, taking into account Poisson noise in these numbers.

Therefore the difference between H-ATLAS ETG detections and the mock HeViCS detections at H-ATLAS distances, is greater than 11σ. This corresponds to a negligible probability ($<10^{-28}$) of the HeViCS sample being consistent with the H-ATLAS sample, in terms of their intrinsic submm properties. Thus the differences in specific dust distributions seen in Fig. 8 is not explained by different dust mass detection limits in the two samples.

6.2 Environments

As it has been shown that MAGPHYS successfully reproduces the modBB results for dust mass, we adopt hereafter the parameters ($T_{\rm d}$, $M_{\rm d}$ and M_*) derived with MAGPHYS. This has the advantage of ensuring uniformity of approach and also of providing SF parameters. However, this means that we must exclude from the subsequent analysis the four HeViCS ETG with synchrotron radiation and the MAGPHYS PF (4 in HeViCS and 11 in H-ATLAS). We note that the multiwaveband photometric data sets used in the MAGPHYS fits are different for the HeViCS and H-ATLAS samples. We begin by examining the relationship between environment and dust-to-stellar mass ratio in Fig. 11. In spite of the large scatter in this plot, there is a weak overall log–log anticorrelation ($r_P = -0.3$), which is influenced by the different sensitivity limits of the two samples. For H-ATLAS data alone, the correlation coefficient decreases to $r_P = -0.2$, which is not a significant result, therefore the anticorrelation is not clear within each individual sample.

For the H-ATLAS sample, which is less sensitive, we have attempted a stacking analysis to probe the undetected ETG (following the methods of Bourne et al. 2012), accounting for blending of nearby sources and assuming the flux is spread out over the optical extent of each source (Hill et al. 2011). By stacking at the position

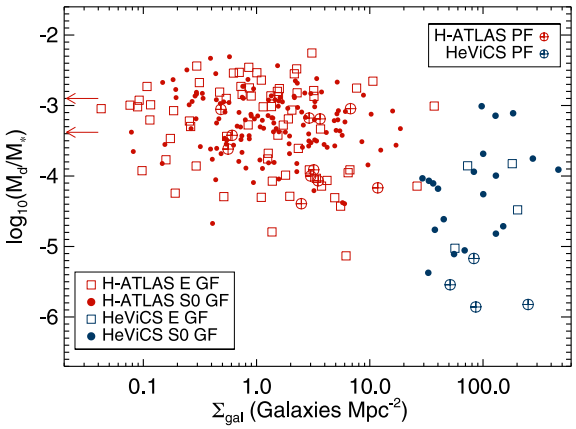

Figure 11. Dust-to-stellar mass ratio derived from MAGPHYS fits plotted against environment surface density for the two ETG samples. H-ATLAS ETG are plotted in red (Es are open circles and S0s are filled circles) and HeViCS ETG are plotted in blue (Es are open squares and S0s are filled squares). Poor SED fits are marked in encircled crosses (in red or blue based on the sample). Arrows indicate the dust-to-stellar mass ratio for two H-ATLAS S0s at $\Sigma_{\rm gal}$ =0.001 gals Mpc^{-2}.

of the undetected ETG in the 100–500 μm maps, we derive the median value of the flux density in the stack in order to avoid bias from outliers, and we estimate the 1σ error on the median from the distribution of values in the stack. From these median stacked flux densities, we find a median dust mass of $\sim$4.44 $\times 10^5$ M$_\odot$, at a median surface density of $\Sigma_{\rm gal} = 2.3$ gals Mpc^{-2} and median stellar mass of $\sim 2.0 \times 10^{10}$ M$_\odot$. This is at $\log_{10}(M_*) = 10.3$ and $\log_{10}(M_{\rm d}/M_*) = -4.65$, which lies amongst the dust detected S0 galaxies in the Virgo cluster in Fig. 8 and well above the HeViCS detection limits. In Fig. 11, this specific dust mass is comparable to the Virgo detected ETG. However, the 90 undetected ETG in the Virgo cluster will lie well below this point in specific dust mass, since they are below the dashed blue lines in Fig. 8 and the two samples cover similar stellar mass ranges. Conversely, if the detected Virgo ETG were placed at the average distance of the GAMA ETG sample, then only one Virgo ETG would be detected in Fig. 11 (VCC1535). It is difficult to quantify the lower limit of the distribution in Fig. 11 without further constraints, but it is clear that sensitivity limits are not causing the downward slope seen at the top of the distribution in Fig. 11.

The substantial range of normalized dust mass displayed by the Virgo ETG is a feature which needs to be subjected to more scrutiny, e.g. studying the dust detection rate and normalized dust mass in fast- and slow-rotators, following a suggestion by S13. ATLAS^{3D} is an ongoing survey investigating the kinematic properties of a volume-limited sample of ETG including the Virgo cluster, finding that elliptical galaxies tend to be either slow rotators or rotate faster than lenticulars (based on apparent specific angular momentum). They find that non-rotating ETG tend to be found in highly overdense environments (Krajnović et al. 2011) – their results also indicate that in dense groups and clusters gas accretion is suppressed. Although 20 of the ETG in the HeViCS sample correspond with those studied by ATLAS^{3D} (Emsellem et al. 2011), it is inconclusive from such a comparison whether the rotation speed of each galaxy is related to its respective dust-to-stellar mass ratio, for the current sample. However, it has been shown that a galaxy's stellar angular momentum and stellar mass are negatively correlated (e.g. Emsellem et al. 2011), and normalized dust mass is negatively correlated with stellar mass (A13). Therefore, it can be postulated

that dust-to-stellar mass ratio is positively correlated with a galaxy's rotation speed. However, the reverse trend was found in Virgo (S13), probably because in a denser environment the giant slow rotators may be collectors of stripped dust. This suggestion might be investigated in the future with high-resolution, kinematic observations of the cold dust or gas in GAMA/H-ATLAS ETG.

Given the wide range of environments inhabited by the H-ATLAS ETGs, and the large sample size, we can now split H-ATLAS ETG into two subsamples: H-ATLAS-LOW ($\Sigma_{\rm gal}$ <1.25 gals Mpc^{-2}) and H-ATLAS-HIGH ($\Sigma_{\rm gal}$ ≥1.25 gals Mpc^{-2}).[8] Note that such subsampling is not possible for HeViCS ETGs due to the small sample size. We examine average MAGPHYS dust-to-stellar mass ratio for the two subsamples, and subsequently compare with HeViCS dust-to-stellar mass.

H-ATLAS-HIGH has a mean dust-to-stellar mass ratio of $\log_{10}(M_{\rm d}/M_*) = -3.35$, indicating lower dust fractions on average in comparison to H-ATLAS-LOW (mean $\log_{10}(M_{\rm d}/M_*) = -3.19$). This may be influenced by the well-known property that massive ETG tend to reside in denser environments. In fact H-ATLAS-HIGH has intermediate dust-to-stellar mass ratio between H-ATLAS-LOW and HeViCS (mean $\log_{10}(M_{\rm d}/M_*) = -4.55$). However, a KS test indicates no significant difference in the distribution of this parameter between the two H-ATLAS subsamples.

These results for dust parameters can be interpreted in different ways. The subtle decrease in relative dust mass with increasing environment may be a real effect, which is then extended to the dense region of the Virgo cluster, or it may be completely spurious. Our tests using mock catalogues above confirms the real difference between the two samples. More samples at intermediate environment densities and in other cluster environments are needed to test the reality of this trend with environment.

6.3 SF properties

In A13, UV-optical colour was used as a proxy for SFR in a galaxy. However blue UV-optical colours can also be induced by the presence of a very old stellar population in the galaxy (Greggio & Renzini 1990; Horch, Demarque & Pinsonneault 1992; Bressan, Chiosi & Fagotto 1994) and therefore further investigation of the SFRs in these galaxies is a necessity to confirm the results found thus far. This must be handled with care, as SFRs derived from MAGPHYS are also related to the UV emission; however the inclusion of longer wavelength information and energy balance in SFR calculations gives a better estimation than a simple proxy. Additionally, it should be noted that SFR estimates using FIR data are subject to large errors in galaxies where dust heating is dominated by the diffuse radiation field from an old stellar population (Bendo et al. 2012).

The interpretation of SED fits to ETG data must account for the potential contribution to UV light from old, evolved stars on the horizontal branch (HB). Burstein et al. (1988) showed that populations of stars older than ∼10 Gyr can cause an upturn in the UV flux, due to UV emission from HB stars. Younger populations do not have this component contributing to the integrated UV light. Populations younger than ∼3 Gyr again have excess UV emission but from the young, massive, main-sequence stars. Thus all intermediate age populations (∼3–10 Gyr) do not have significant UV upturns in their spectra and hence will show no sign of a UV excess that could be erroneously attributed to the presence of young stars. The *GALEX* NUV flux is less affected by the UV flux from old, evolved stars than the *GALEX* FUV band (see Kaviraj et al. 2007, their fig. 1).

A concern with using MAGPHYS for the interpretation of parameters such as SFR, is that they are based on optical, UV and FIR emission and are calibrated only for galaxies where dust heating is primarily contributed to from the young and old stellar population. However, if the photons heating the dust come primarily from UV emission from an old stellar population, then the results obtained with MAGPHYS are less reliable, because of the uncertainty in UV contribution from old stars. This is a known effect, which is partly incorporated into the models of Bruzual & Charlot (2003) used in MAGPHYS, through the (albeit uncertain) inclusion of some hot evolved stars. Salim et al. (2007, and references therein) tested nearby elliptical galaxies, also using the models of Bruzual & Charlot (2003) and found that those models could account for UV light from old stellar populations. In addition, eyeballing the fits done here indicates that the UV upturn of the ETG is not a strong effect.

We can further strengthen our argument that UV emission from the old stellar population is not the driving mechanism for the dust heating by examining the NUV-r colour, in relation to that expected from the UV upturn. UV contamination from old stars leads to colours that are still redder than NUV-r>5.0 (from the sample of Kaviraj et al. 2007; their fig. 11). Their ETG classified as old (ages>1 Gyr from stellar population model fits) all have NUV-r>5.0. For example, NUV-r = 5.4 is the colour of the strong UV-upturn galaxy NGC 4552 (see Yi et al. 2005). In the H-ATLAS/GAMA sample 141 out of 184 NUV detected ETG are bluer than NUV-r = 5.0. This large fraction of blue NUV-r ETG in the A13 sample indicates that the blue colours cannot be explained by a UV upturn from old, evolved stars alone. Therefore, the blueness and large scatter of their NUV-r colours (ranging from ∼1.5 to 6.5) indicates that these colour and UV fluxes are dominated by different amounts of recent SF in these ETG rather than by UV emission from old, evolved stars. However, we note that for up to 36 per cent of the 220 dust detected ETG in A13 (including 43 with NUV-r>5.0 plus 36 NUV non-detections) the UV radiation and dust heating could be dominated by old stars, making their MAGPHYS SF rates overestimates. The fractional mass involved in the SF does not need to be very large in order to strongly influence the NUV-r colours of stellar populations (see review by Kaviraj 2008, their fig. 1).

The 33 ETG in the HeViCS sample do not exhibit such blue colours, with the average NUV-r∼5.3. Also di Serego Alighieri (2013) has shown that dust-detected HeViCS ETG are not bluer in B–H colour than the undetected ones. These facts should be kept in mind when considering the parameters extracted based on MAGPHYS fits to these galaxies, and may in fact result in SFR overestimates for Virgo Cluster ETG.

We examine the sSFR (defined in Section 5.1) as derived by MAGPHYS below. Fig. 12 shows sSFR plotted against stellar mass, where a similar trend to Fig. 8 emerges in the form of an anticorrelation between sSFR and stellar mass of the ETG for the two samples. Regression lines are fit to the two samples, revealing correlation coefficients of r_P =−0.572 and −0.733 for H-ATLAS and HeViCS samples, respectively. These are both significant with much less than 1 per cent probability of occurring by chance. As expected, since derived dust mass and SFR are both influenced by the FIR flux, this corresponds to what was observed for dust-to-stellar mass: H-ATLAS ETG show a weaker correlation for dust-to-stellar mass and sSFR against stellar mass in comparison to HeViCS. Those

[8] The environment cutoff has been chosen to create subsamples of equivalent size

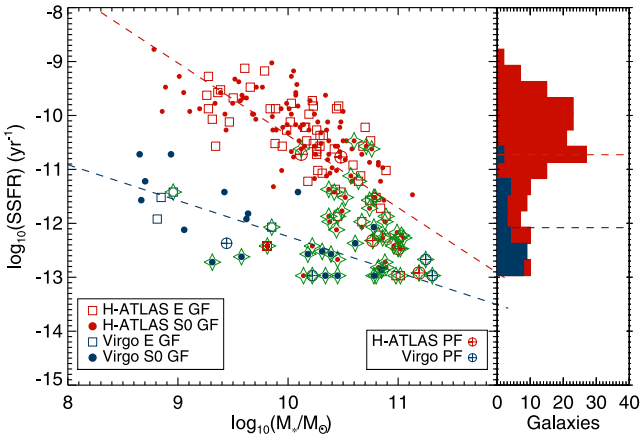

Figure 12. MAGPHYS derived sSFR plotted against stellar mass for the two ETG samples. See Fig. 11 for symbols and labels. Green stars overplot points with NUV-r>5. Red and blue dashed lines show best linear fits to H-ATLAS and HeViCS, respectively. Histograms of these distributions are plotted on the right.

galaxies with NUV-r>5.0 are indicated by green stars in Fig. 12. This gives an indication of which points are most likely to be upper limits rather than full SFR measurements in this plot and most of these occur at higher stellar masses. Future work is required to more accurately constrain the low sSFRs occurring in massive ETG.

The side panel of Fig. 12 shows the distribution of galaxies in sSFR space for the two samples. This quite clearly identifies the higher-on-average sSFR for H-ATLAS ETG compared with HeViCS ETG, further strengthening the point that H-ATLAS ETG are not only dusty, but actively star forming. The most star-forming end of this distribution displays sSFRs which exceed that of our Milky Way Galaxy.

This anticorrelation between sSFR and stellar mass has previously been observed in both the local and medium-redshift Universe (Salim et al. 2007; Somerville et al. 2008; Firmani, Avila-Reese & Rodríguez-Puebla 2010). The study by Salim et al. (2007) took observations of 50 000 SDSS galaxies with a range of morphologies and stellar masses and, after measuring their sSFRs using synthetic population models including dust attenuation, constrained this relation to purely star-forming galaxies as

$$\log(sSFR) = -0.35 \log M_* - 6.33. \quad (3)$$

Those star-forming galaxies covered $\log(M_*/\mathrm{M}_\odot) \sim 8.4$–$11.3$ and $\log(sSFR) \sim -8.6$ to -10.9. In contrast with this, and over a similar range in stellar mass, the HeViCS ETG display a slightly steeper slope with

$$\log(sSFR) = -0.59 \log M_* - 6.39 \quad (\mathrm{NUV-r} = \mathrm{all}) \quad (4)$$

$$\log(sSFR) = -0.39 \log M_* - 8.02 \quad (\mathrm{NUV-r} < 5.0) \quad (5)$$

and the H-ATLAS ETG produce the steepest gradient of all with

$$\log(sSFR) = -1.37 \log M_* + 3.40 \quad (\mathrm{NUV-r} = \mathrm{all}) \quad (6)$$

$$\log(sSFR) = -0.90 \log M_* - 1.20 \quad (\mathrm{NUV-r} < 5.0). \quad (7)$$

These differences may be attributed to both the larger sample size and the different galaxy types (presumably dominated by later type galaxies) making up the relation in Salim et al. (2007). For the HeViCS and H-ATLAS samples, we give above the relations both with and without the green points shown in Fig. 12 (NUV-r>5.0), since those points indicate the least certain associations with ongoing SF. Irrespective of whether those points are included or not, the ETG used in our work span a large range of sSFRs and the relation's gradient is likely to be steepened by the extreme sSFR values. Such a steep relation for the H-ATLAS ETG, coupled with the extreme levels of dust content for lower stellar mass H-ATLAS ETG, is consistent with sSFR downsizing where lower mass ETG harbour SF in even the local Universe. These low-mass ETG also occupy the sparsest environments ($\leq$1 galaxy Mpc^{-2}), further strengthening this downsizing theory and in accordance with previous results shown for galaxies in the local Universe (Cassata et al. 2007; Cooper et al. 2007; Wijesinghe et al. 2012).

What we are seeing in the H-ATLAS ETG sample are galaxies like the rejuvenated ones proposed in Thomas et al. (2010, see also Young et al. 2014). These rejuvenated ETG have some recent SF as well as old stars and are increasingly common with decreasing galaxy mass. Thomas et al. (2010) postulate, from trends seen in SDSS data, with environment and chemistry, that these cases, with contributions from relatively recent SF, are decisively influenced by environment. They support their claim of rejuvination with observations that show that the more recent SF is less enhanced in [α/Fe], and has thus had time to build up more iron from Type-Ia supernova, for the composition of the later starburst, in contrast to the older stars. This trend with environment is similar to the results that we find here. Their fig. 8 shows that this is particularly significant for low-mass ETGs, as we find in Fig. 12.

Models for downsizing predict that lower mass galaxies have more extended SFHs (e.g. De Lucia et al. 2006). If the H-ATLAS sample is divided into low-mass ($M_* < 10^{10.5}$ M$_\odot$) and high-mass systems ($M_* \geq 10^{10.5}$ M$_\odot$), it is interesting to note that the lower mass systems exhibit higher average sSFRs over the full redshift range (consistent with results by Firmani et al. 2010). Additionally the higher mass systems show the most similar sSFR to the average sSFR of the HeViCS ETG, indicating greater similarity between these systems than the lower mass ETG have with either of these groupings.

6.4 Age properties

Ideally, an exploration of the ages of these ETG would begin by using spatially resolved, population synthesis modelling for these systems as a whole. In the case of the H-ATLAS ETG this has not been done yet because current imaging does not have good enough resolution. Therefore, we choose to run a pilot study on the ages of these galaxies using MAGPHYS results. Caution must be applied to the use of these results, as they are fully dependent on SPS code used to compute the short-wavelength light produced by stars, which is likewise dependent on the model's choice of metallicity, IMF and SFH. In this case, the SPS code is that of Bruzual & Charlot (2003), and they adopt a range of exponentially declining SFHs plus bursts and a Chabrier IMF (Chabrier 2003). Here, we will only consider relative numbers, and not absolute ages.

We choose to examine two forms of galactic age: the formation time-scale (T_{form}), which is defined as the age of the oldest stars in the galaxy and is a good representative of the age of the galaxy, and the time the last burst of SF ended (T_{lastb}). The distributions of both these parameters and means thereof are compared in Fig. 13. Probability results from KS testing the distributions are also included in these figures. The left-hand panel indicates that the two samples have significantly different formation time-scales. However,

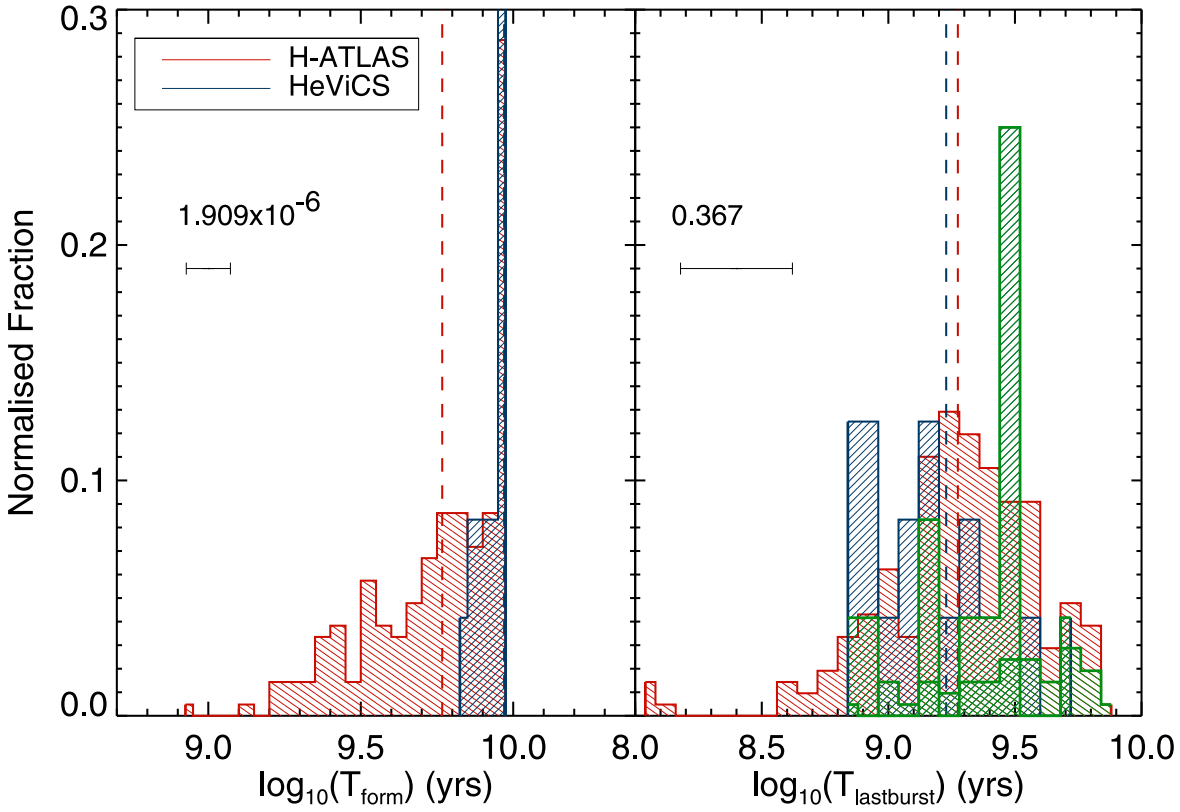

Figure 13. Distributions of $T_{\rm form}$ (left) and $T_{\rm lastb}$ (right) for H-ATLAS (red) and HeViCS (blue) populations. Numbers in the plots represent KS probabilities of parameter distributions coming from the same parent sample. Dashed lines represent mean values in the samples' respective colours. Error bars represent the mean 1σ errors for both samples. For $T_{\rm lastb}$ (right) galaxies with NUV-r>5.0 are indicated with green histograms.

the results for $T_{\rm lastb}$ indicate that there is no difference (<1 per cent probability of a difference) between the two sets of galaxies. This is an interesting result as it is the first point at which any similarity between the parameters of the two sets of ETG has been found, although $T_{\rm lastb}$ is not always well determined. The green histograms plotted for $T_{\rm lastb}$ in the right plot in Fig. 13 illustrate where the least certain measurements are, since these have NUV-r>5.0 colours. These time-scales are provisional estimates, compared here in a relative way. Further detailed study on the galactic stellar populations is required to determine whether these results are real or simply a result of the assumptions made in the SPS fitting.

6.5 Additional considerations

Based on the results discussed above, a clear conclusion about the two samples is reaffirmed: that the ETG in each of the samples have differing dust properties, with HeViCS ETG demonstrating consistently low dust levels, whilst the H-ATLAS ETG have significantly higher dust levels which bridge the gap between HeViCS ETG and late-type spirals. The dust-to-stellar mass ratio is shown to be strongly driven by the stellar mass of the galaxy, particularly for the HeViCS systems. This work has made uniform the calculations of stellar and dust mass for two samples; this has served to strengthen the result that there is almost no overlap between dust-to-stellar mass ratio for fixed stellar mass for ETG from these two samples, covering different environments.

This lack of overlap results partly from different dust detection limits between the two samples; the closer distance to HeViCS ETG and deeper observations result in much lower detectable dust levels in the HeViCS sample. From the H-ATLAS Science Demonstration Phase (Rowlands et al. 2012) stacked 233 optically selected ETG from GAMA and found that they have average dust masses of an order of magnitude less than their H-ATLAS detected ETG. However, this does not explain why there are no HeViCS ETG occupying the same regions as the H-ATLAS submm detected ETG. This cannot be explained by a detection limit, but may be due to the larger area surveyed by H-ATLAS. Some of the more extreme cases in H-ATLAS could be explained as unusual ETG, but given that all H-ATLAS ETG occupy the top region of Fig. 8, this effect is likely explained by the difference in environment. Alternatively, this could be caused by the inability of dust to survive in dense environments due to galaxy–cluster interactions. Hydrodynamical or gravitational interactions that are likely to occur in dense regions may shorten the lifetime of dust, as may hot gas in the hostile intracluster medium.

There are only three HeViCS ETG which demonstrate normalized dust masses on a level with the H-ATLAS ETG (VCC 327, 450 and 571). These all have GOLDMine classifications of S0 and are found in high-density regions of Virgo ($\Sigma_{\rm gal}$ ∼100–200 gals Mpc^{-2}). It may be possible that these galaxies have been recently accreted into the Virgo cluster (e.g. Kraft et al. 2011), and have not yet been subjected to the effects of dust stripping and destruction in the intracluster medium.

We run a simple test to check whether this may be a possibility. Based on Virgo infall velocities provided by Mould et al. (2000) and assuming a Virgo cluster radius of 2.2 Mpc (Mei et al. 2007), we calculate typical crossing times for these three Virgo ETG of ∼0.7, 0.8 and 2.2 Gyr. If we assume ram-pressure stripping is

responsible for the majority of dust loss in Virgo ETG, with typical removal time-scales of a few $\times$ 10^8 yr (Takeda, Nulsen & Fabian 1984; Murakami & Babul 1999), then it may be possible to relate these high relative dust levels with recent galactic infall into the Virgo cluster. These relatively short crossing times illustrate that the current local density may not be the same as the time averaged local density experienced by a galaxy in the Virgo cluster. This is in contrast to what happens in the field. This may contribute to the different behaviours with environment shown in Fig. 5.

Dust masses detected in these galaxies can be used to estimate total (both atomic and molecular) gas mass: a typical gas-to-dust ratio of 100 (e.g. Parkin et al. 2012) gives a range of $\sim 1 \times 10^7$–8×10^9 $M_\odot$ for the H-ATLAS sample and $\sim 10^6$–5×10^8 $M_\odot$ in HeViCS. ATLAS^{3D} estimate molecular gas mass for some of the Virgo galaxies in this sample, finding an upper limit of $10^{8.59}$ $M_\odot$ for these particular galaxies (Young et al. 2011), which is consistent with our estimations for total gas mass. Additional results from ATLAS^{3D} find a strong H I detection rate dependence on surface density whereby H I in ETG is preferentially detected outside the Virgo Cluster (Serra et al. 2012); again these results are qualitatively consistent with our findings for the two samples whereby H-ATLAS ETG demonstrate a factor of 10 dust and hence gas mass higher than HeViCS ETG in the dense regions of Virgo. However, while we note that dust and gas masses are both low in these Virgo ETG, S13 found that dust and H I detections in Virgo ETG showed very small overlap, counter to the assumption that dust follows gas mass.

Similar studies run on samples of LTG in the Virgo Cluster have demonstrated appreciably low levels of H I gas compared to LTG in sparser environments. Additionally, lower SF activity has been identified in these spiral galaxies, and possibly lower dust levels (Boselli & Gavazzi 2006 and references therein). Models indicate that ram pressure stripping, gas compression (Byrd & Valtonen 1990; Tonnesen & Bryan 2009) and starvation due to the cluster potential (Balogh, Navarro & Morris 2000) are possible causes of these decreased levels of gas and dust in LTG. Theoretically, ETG in the same environment would also be subjected to these same physical mechanisms, resulting in the lower levels of gas and dust currently being observed.

The HRS (Boselli et al. 2010a) sampled a wider range of galaxy environments than just the Virgo cluster. Although it includes very few luminous ETG other than those in the Virgo cluster, it is still useful to consider where their ETG reside in terms of parameter space, and how this compares to the two samples investigated here. Smith et al. (2012) find 31 ETG in the HRS parent sample with 250 μm detections: these all have stellar masses at $\gtrsim 10^{10}$ $M_\odot$ and modBB fits to the sample reveal a dust mass range of $10^{5.0–7.1}$ $M_\odot$ and dust temperatures of 16–32K. Most notably, however, while they find a similar trend for dust-to-stellar mass ratio with stellar mass, their elliptical galaxies are found to present the lowest normalized dust masses. This is not what is seen here, particularly for the H-ATLAS/GAMA sample. It should be noted that the HRS sample only contains seven submm detected elliptical galaxies, and therefore this result may be due to poor statistics. The majority ($\sim$68 per cent) of the HRS ETG reside within the Virgo cluster, which explains the similar dust mass range to that of the HeViCS survey; in fact Smith et al. (2012) explicitly state that there is overlap between their ETG and those of S13. Therefore, we choose not to include a further study with HRS ETG.

In summary, we find tentative evidence that specific dust mass depends broadly on environment, however, more galaxy samples at intermediate environment density are needed to confirm such a trend.

7 CONCLUSIONS

This work has compared H-ATLAS submm detected ETG to HeViCS (Virgo Cluster) submm detected ETG. This was a strongly motivated study, as multiple *Herschel* works have revealed different levels of dust in different samples of ETG (Skibba et al. 2011; Smith et al. 2012; Rowlands et al. 2012; S13; A13). It has been unclear thus far whether these differences are simply due to different sample statistics and/or selection effects, or whether they are real differences which are a result of the different samples observing different types of ETG.

Two samples were selected for this study: the A13 H-ATLAS sample of 220 ETG and 33 ETG from the HeViCS S13 sample, both with $M_r < -17.4$ mag. With the aid of consistent calculations for nearest neighbour density, and MAGPHYS panchromatic SED fitting to the multiwavelength data, we were able to objectively quantify the true differences in the properties of these ETG. The results of this study are summarized here below.

(i) Nearest neighbour surface densities revealed true differences in the type of environment in which these ETG reside. H-ATLAS ETG are in isolated environments, spanning $\lesssim$0.1–10 galaxies Mpc^{-2}, whereas HeViCS ETG are dominated by the cluster environment ($\sim$25–500 galaxies Mpc^{-2}). These results are also true for undetected ETG in each sample, with only a trace overlap in density between samples observed at $\sim$20–100 galaxies Mpc^{-2}. We find that submm detected ETG in H-ATLAS reside in sparser environments than undetected ETG.

(ii) ModBB fits from A13 and S13 reveal different ranges of dust-to-stellar mass ratio, with H-ATLAS ETG demonstrating higher M_d/M_* at fixed stellar mass. We prove that this is not a selection effect by carrying out a KS test and by Monte Carlo simulations of Virgo ETG at GAMA ETG distance. Both these tests confirm that the samples have <0.1 per cent probability of having been drawn from the same specific dust mass distribution.

(iii) MAGPHYS results indicate that it is sometimes difficult to accurately constrain the cold dust temperature, but similar results for dust mass were obtained using MAGPHYS and ModBB fits, in spite of these uncertainties. ModBB fits appear to give higher dust mass of a galaxy in some cases – this may be because the smaller dust grains which emit at higher temperatures are not accounted for in the ModBB fits.

(iv) MAGPHYS stellar masses including UKIDSS fluxes are lower than those produced by Zibetti et al. (2009, HeViCS) and the GAMA team (Taylor et al. 2011, H-ATLAS). Both sets of stellar masses indicate that H-ATLAS ETG are more massive on average than HeViCS ETG.

(v) Correlations are found between dust mass and stellar mass for both H-ATLAS ($r_P = 0.42$) and HeViCS ($r_P = 0.58$) ETG. Additionally, anticorrelations are found between dust-to-stellar mass ratio and stellar mass, although the trend is shifted upwards (to higher normalized dust mass) for H-ATLAS. Most of this anticorrelation is due to the dust detection limits. However, it remains to be understood why there is a lack of massive ETG in Virgo with high dust-to-stellar mass ratios. Investigating dust-to-stellar mass ratio as a function of nearest neighbour density reveals another correlation between the two properties, where both H-ATLAS and HeViCS ETG sit on the same trendline. This is an indicator that levels of dust mass in ETG are affected by their environments.

(vi) Examinations of sSFR reveal that dust mass is indicative of ongoing SF in many of these galaxies, but is not directly related, as evidenced by different trends in specific dust mass and sSFR plots with stellar mass. It appears that there is very little (if any) ongoing

SF in the HeViCS ETG, but quite the opposite is true for a large proportion of the H-ATLAS sample, with the highest sSFRs on par with that of spiral galaxies.

(vii) The massive ETG in H-ATLAS have similar sSFRs to the HeViCS ETG.

ACKNOWLEDGEMENTS

We would like to acknowledge and thank Elisabete da Cunha for her contribution of modified MAGPHYS libraries. NKA acknowledges the support of the Science and Technology Facilities Council. LD, RJI and SJM acknowledge support from the European Research Council Advanced Grant COSMICISM. IDL gratefully acknowledges the support of the Flemish Fund for Scientific Research (FWO-Vlaanderen). KR acknowledges support from the European Research Council Starting Grant SEDmorph (P.I. V. Wild). The *Herschel*-ATLAS is a project with *Herschel*; which is an ESA space observatory with science instruments provided by European-led Principal Investigator consortia and with important participation from NASA. The H-ATLAS web site is http://www.h-atlas.org/. GAMA is a joint European-Australasian project based around a spectroscopic campaign using the AAT. The GAMA input catalogue is based on data taken from the SDSS and UKIRT Infrared Deep Sky Survey. Complementary imaging of the GAMA regions is being obtained by a number of independent survey programmes including *GALEX* MIS, VST KIDS, VISTA VIKING, *WISE*, *Herschel*-ATLAS, GMRT and ASKAP providing UV to radio coverage. GAMA is funded by the STFC (UK), the ARC (Australia), the AAO, and the participating institutions. The GAMA web site is http://www.gama-survey.org/. We thank Gianfranco De Zotti and Michal Michalowski for helpful comments on an earlier draft of this paper. Thanks to the anonymous referee for useful suggestions that improved the paper.

REFERENCES

Abazajian K. N. et al., 2009, ApJS, 182, 543
Amblard A., Riguccini L., Temi P., Im. S., Fanelli M., Serra P., 2014, ApJ, 783, 135
Agius N. K. et al., 2013, MNRAS, 431, 1929 (A13)
Auld R. et al., 2013, MNRAS, 428, 1880
Baldwin J. A., Phillips M. M., Terlevich R., 1981, PASP, 93, 5
Balogh M. L., Navarro J. F., Morris S. L., 2000, ApJ, 540, 113
Bendo G. J. et al., 2012, MNRAS, 419, 1833
Bianchi S., 2013, A&A, 552, A89
Bianchi L., GALEX Team, 1999, Mem. Soc. Astron. Ital., 70, 365
Binggeli B., Sandage A., Tammann G. A., 1985, AJ, 90, 1681
Binggeli B., Popescu C. C., Tammann G. A., 1993, A&AS, 98, 275
Blain A. W., Barnard V. E., Chapman S. C., 2003, MNRAS, 338, 733
Boselli A., 2012, in Boissier S., de Laverny P., Nardetto N., Samadi R., Valls-Gabaud D., Wozniak H., eds, Proceedings of the Annual meeting of the French Society of Astronomy and Astrophysics. Société Française d'Astronomie et d'Astrophysique, p. 435
Boselli A., Gavazzi G., 2006, PASP, 118, 517
Boselli A. et al., 2010a, PASP, 122, 261
Boselli A. et al., 2010b, A&A, 518, L61
Boselli A. et al., 2011, A&A, 528, A107
Bourne N. et al., 2012, MNRAS, 421, 3027
Bressan A., Chiosi C., Fagotto F., 1994, ApJS, 94, 63
Brough S. et al., 2013, MNRAS, 435, 2903
Bruzual G., Charlot S., 2003, MNRAS, 344, 1000
Burstein D., Bertola F., Buson L. M., Faber S. M., Lauer T. R., 1988, ApJ, 328, 440
Byrd G., Valtonen M., 1990, ApJ, 350, 89
Cassata P. et al., 2007, ApJS, 172, 270
Chabrier G., 2003, PASP, 115, 763
Charlot S., Fall S. M., 2000, ApJ, 539, 718
Ciesla L. et al., 2014, A&A, 565, A128
Cooper M. C. et al., 2007, MNRAS, 376, 1445
Cortese L. et al., 2010a, A&A, 518, L49
Cortese L. et al., 2010b, A&A, 518, L63
Cortese L. et al., 2012a, A&A, 540, A52
Cortese L. et al., 2012b, A&A, 544, A101
da Cunha E., Charlot S., Elbaz D., 2008, MNRAS, 388, 1595
Dale D. A. et al., 2012, ApJ, 745, 95
Davies J. I. et al., 2010, A&A, 518, L48
Davies J. I. et al., 2012, MNRAS, 419, 3505
Davies J. I. et al., 2014, MNRAS, 438, 1922
Davis T. A. et al., 2013, MNRAS, 429, 534
De Lucia G., Springel V., White S. D. M., Croton D., Kauffmann G., 2006, MNRAS, 366, 499
di Serego Alighieri S., 2013, in Thomas D., Pasquali A., Ferreras I., eds, Proc. IAU Symp. 295, The Intriguing Life of Massive Galaxies. Kluwer, Dordrecht, p. 332
di Serego Alighieri S. et al., 2007, A&A, 474, 851
di Serego Alighieri S. et al., 2013, A&A, 552, A8 (S13)
Draine B. T., 2003, ARA&A, 41, 241
Dressler A., 1980, ApJ, 236, 351
Driver S. P. et al., 2011, MNRAS, 413, 971
Dunne L., Eales S. A., 2001, MNRAS, 327, 697
Dunne L., Eales S., Edmunds M., Ivison R., Alexander P., Clements D. L., 2000, MNRAS, 315, 115
Dunne L. et al., 2011, MNRAS, 417, 1510
Dye S. et al., 2010, A&A, 518, L10
Eales S. et al., 2010, PASP, 122, 499
Emsellem E. et al., 2011, MNRAS, 414, 888
Ferrarese L. et al., 2012, ApJS, 200, 4
Firmani C., Avila-Reese V., Rodríguez-Puebla A., 2010, MNRAS, 404, 1100
Galametz M. et al., 2011, in Alecian G., Belkacem K., Samadi R., Valls-Gabaud D., eds, Proceedings of the Annual meeting of the French Society of Astronomy and Astrophysics. Société Française d'Astronomie et d'Astrophysique p. 119
Gavazzi G., Boselli A., Donati A., Franzetti P., Scodeggio M., 2003, A&A, 400, 451
Gomez H. L. et al., 2010, A&A, 518, L45
Greggio L., Renzini A., 1990, ApJ, 364, 35
Griffin M. J. et al., 2010, A&A, 518, L3
Gutermuth R. A., Megeath S. T., Pipher J. L., Williams J. P., Allen L. E., Myers P. C., Raines S. N., 2005, ApJ, 632, 397
Hill D. T. et al., 2011, MNRAS, 412, 765
Hopkins A. M. et al., 2013, MNRAS, 430, 2047
Horch E., Demarque P., Pinsonneault M., 1992, ApJ, 388, L53
Ibar E. et al., 2010, MNRAS, 409, 38
Janowiecki S., Mihos J. C., Harding P., Feldmeier J. J., Rudick C., Morrison H., 2010, ApJ, 715, 972
Jarrett T. H. et al., 2011, ApJ, 735, 112
Jarrett T. H. et al., 2013, AJ, 145, 6
Kaviraj S., 2008, Mod. Phys. Lett. A, 23, 153
Kaviraj S., Rey S.-C., Rich R. M., Yoon S.-J., Yi S. K., 2007, MNRAS, 381, L74
Kelvin L. S. et al., 2014, MNRAS, 439, 1245
Kenney J. D. P., Tal T., Crowl H. H., Feldmeier J., Jacoby G. H., 2008, ApJ, 687, L69
Kraft R. P. et al., 2011, ApJ, 727, 41
Krajnović D. et al., 2011, MNRAS, 414, 2923
Lawrence A. et al., 2007, MNRAS, 379, 1599
Mei S. et al., 2007, ApJ, 655, 144
Mould J. R. et al., 2000, ApJ, 529, 786
Muñoz-Mateos J. C. et al., 2009, ApJ, 703, 1569

Murakami I., Babul A., 1999, MNRAS, 309, 161
Parkin T. J. et al., 2012, MNRAS, 422, 2291
Pascale E. et al., 2011, MNRAS, 415, 911
Pilbratt G. L. et al., 2010, A&A, 518, L1
Poglitsch A. et al., 2010, A&A, 518, L2
Pope A. et al., 2006, MNRAS, 370, 1185
Rigby E. E. et al., 2011, MNRAS, 415, 2336
Robotham A. S. G. et al., 2011, MNRAS, 416, 2640
Rowlands K. et al., 2012, MNRAS, 419, 2545
Salim S. et al., 2007, ApJS, 173, 267
Serra P. et al., 2012, MNRAS, 422, 1835
Skibba R. A. et al., 2011, ApJ, 738, 89
Smith D. J. B. et al., 2011, MNRAS, 416, 857
Smith M. W. L. et al., 2012, ApJ, 748, 123
Somerville R. S., Hopkins P. F., Cox T. J., Robertson B. E., Hernquist L., 2008, MNRAS, 391, 481
Sutherland W. et al., 2015, A&A, 575, A25
Takeda H., Nulsen P. E. J., Fabian A. C., 1984, MNRAS, 208, 261
Temi P., Brighenti F., Mathews W. G., 2009a, ApJ, 695, 1
Temi P., Brighenti F., Mathews W. G., 2009b, ApJ, 707, 890
Taylor E. N. et al., 2011, MNRAS, 418, 1587
Thomas D., Maraston C., Bender R., Mendes de Oliveira C., 2005, ApJ, 621, 673
Thomas D., Maraston C., Schawinski K., Sarzi M., Silk J., 2010, MNRAS, 404, 1775
Tonnesen S., Bryan G. L., 2009, ApJ, 694, 789
Trinchieri G., di Serego Alighieri S., 1991, AJ, 101, 1647
Wijesinghe D. B. et al., 2012, MNRAS, 423, 3679
Wright E. L. et al., 2010, AJ, 140, 1868
Yi S. K. et al., 2005, ApJ, 619, L111
Young L. M. et al., 2011, MNRAS, 414, 940
Young L. M. et al., 2014, MNRAS, 444, 3408
Zibetti S., Charlot S., Rix H.-W., 2009, MNRAS, 400, 1181

APPENDIX A: *WISE* PHOTOMETRY

The *WISE* has a beam size of 12.0 arcsec (in the *W*4 band) as its coarsest resolution. This means most of the galaxies in the Virgo cluster are extended objects in all *WISE* bands. Magnitudes from the *WISE* Science Archive[9] are based on aperture photometry using an elliptical aperture for each galaxy. Foreground stars are not removed, hence diluting the flux measurements. We therefore opted to compute asymptotic fluxes for all galaxies in our sample, taking special care of the contamination by bright foreground stars.

The images (e.g. Fig. A1) for each galaxy were retrieved from the *WISE* Science Archive. We choose sufficiently large cut-outs from the All-Sky Atlas in order to cover both the galaxy and its close surroundings.

The local background of the galaxy is estimated from 10 boxes of 50 × 50 pixels. Three values are computed from these boxes: (1) a single background value. A sigma clipped mean was derived from all pixels using a 5σ rejection threshold and iterations until convergence. The background value was then subtracted from the image. (2) A pixel-to-pixel background error. This is the mean of the standard deviations on the pixel values in each of the boxes. (3) A large-scale background variation error. This is the standard deviation of the mean values of each of the boxes.

We identify the brightest stars and mask their corresponding pixels so they will be ignored in the further analysis. An elliptical aperture is then determined, following the galaxy's apparent shape on the sky. The angle and ellipticity of this parent aperture will serve as a base for constructing the growth curve. To construct the growth curve for each galaxy and each band, concentric elliptical annuli are created based on the parent aperture. Starting from the centre of the galaxy, each next aperture is a fraction Δa in major axis larger. We set $\Delta a = a/20$, where a is the major axis of the parent aperture. The total flux inside the elliptical shell is estimated by multiplying the median value of all pixels inside the shell with the total number of pixels. In the number of pixels, we also include the amount of masked pixels. This extra step filters out any remaining contribution of foreground stars, while approximating the flux of the galaxy in that shell. As soon as the calculated flux in a shell falls below the background level, the iteration is stopped.

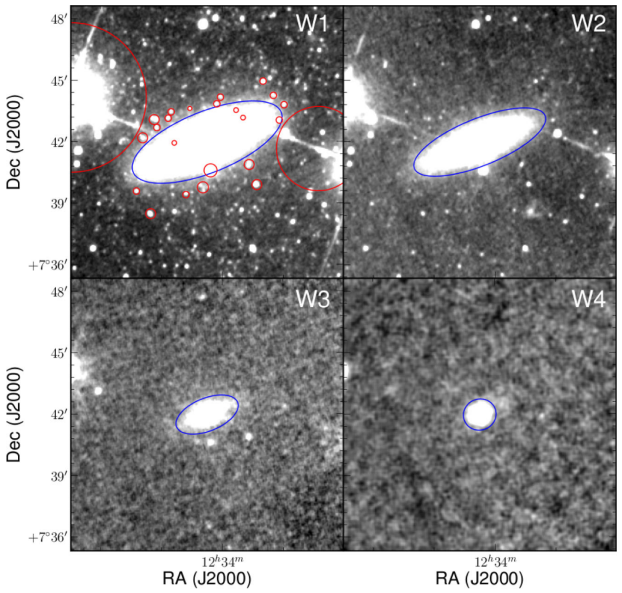

Figure A1. Example galaxy VCC 1535 in all four *WISE* bands. In each frame, the blue ellipse is the parent aperture for that band from which concentric ellipses were derived. In the *W*1 frame (top left), the masked foreground stars are indicated in red circles. These pixels were masked in all bands.

The growth curve is now plotted as the cumulative counts versus the distance to the centre of the galaxy. Following Muñoz-Mateos et al. (2009), the gradient of the growth curve around the edge of the galaxy is calculated. Fig. A2 (lower panel) shows the cumulative counts as a function of this gradient. A linear fit to these points is performed and the intercept with the y-axis is calculated as the asymptotic flux of the galaxy in that particular band. As the gradient changes rapidly and is non-linear inside the parent annulus of the galaxy, these points are not considered in the fit. The outer points of the growth curve are not considered in the fit either, as they are usually dominated by background variations or unmasked foreground stars.

Four sources of uncertainty on the calculated fluxes are considered. (a) The Poisson noise, determined as the square root of the asymptotic flux. A multiplicative factor of 2 for *W*1, *W*2 and *W*3 and 4 for *W*4 must be applied to incorporate the correlated pixel noise, according to the Explanatory Supplement to the *WISE* Preliminary Data Release Products,[10] section II.3.i. (b) The pixel-to-pixel background error as described above. (c) Large-scale background

[9] Science Archive: http://irsa.ipac.caltech.edu

[10] http://wise2.ipac.caltech.edu/docs/release/prelim/expsup/wise_prelrel_toc.html

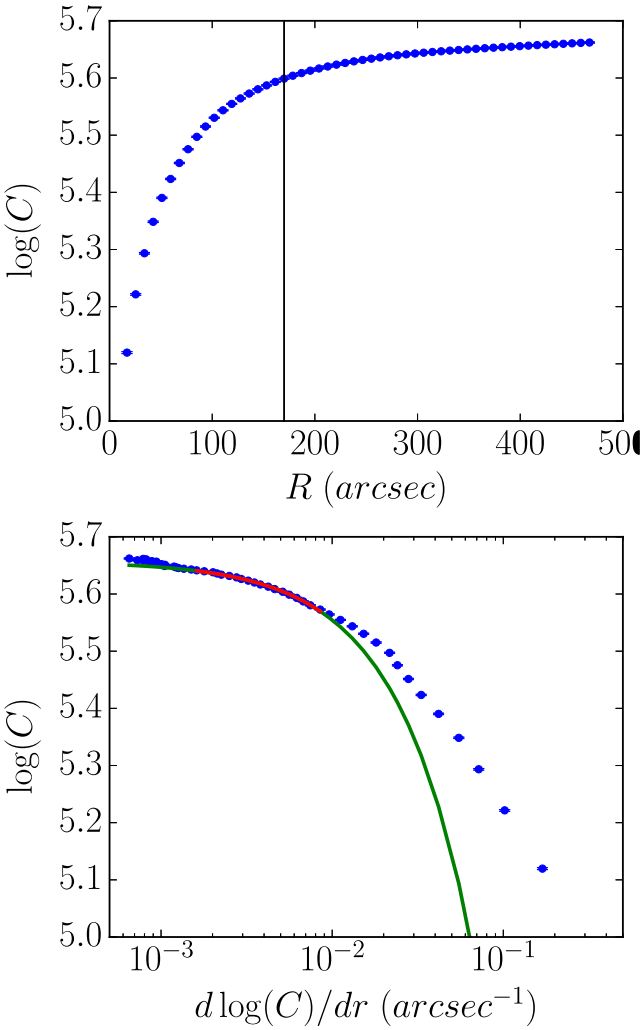

Figure A2. Top: growth curve for the *W*1 band of VCC 1535, showing the log of the cumulative counts for each elliptical shell. The black vertical line indicates the major axis of the parent aperture. Bottom: cumulative counts as a function of the gradient of the growth curve. The red line is a linear fit (displayed here on log-linear scale) to the blue points in that interval. The green line is the extrapolation of this linear fit to all of the points.

variations, also described above. (d) A calibration uncertainty. Following the recommendations of Jarrett et al. (2011), we use 2.4, 2.8, 4.5 and 5.7 per cent as the calibration error in *W*1, *W*2, *W*3 and *W*4, respectively.

The obtained fluxes and their respective errors have to be converted to Jy to be of physical meaning. Section II.3.f of the *WISE* photometry manual,[11] provides the following conversion factors: 1.9350×10^{-6} Jy DN^{-1}, 2.7048×10^{-6} Jy DN^{-1}, 2.9045×10^{-6} Jy DN^{-1} and 5.2269×10^{-6} Jy DN^{-1} for *W*1, *W*2, *W*3 and *W*4, respectively.

Jarrett et al. (2013) advises three corrections to the *WISE* flux of extended sources. One of them is a colour correction, which we do not apply here as our fitting routine takes the filter response

[11] See footnote 10.

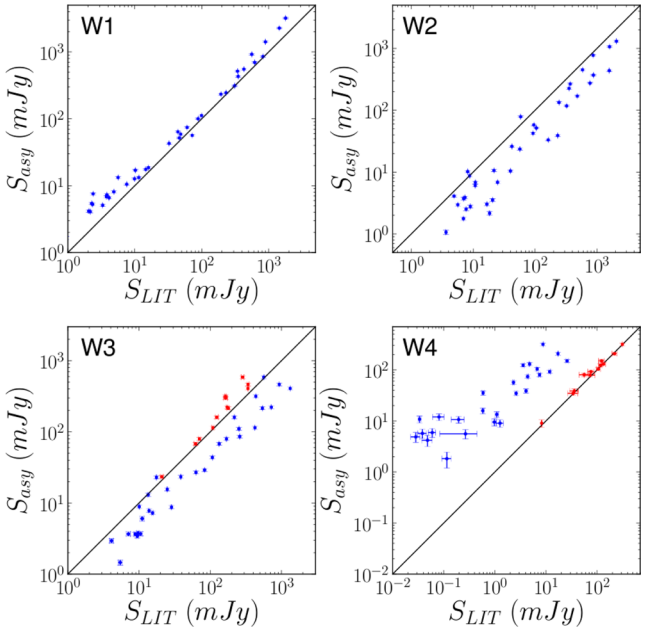

Figure A3. Comparison of the integrated *WISE* fluxes as derived by our method (asymtotic fluxes) and the archival fluxes (blue points) measured from elliptical annuli. Red points are independent photometric measurements in *W*3 and *W*4 from Ciesla et al. (2014) for a subset of our sample. The black line is the 1: 1 relation.

into account. The second correction stems from a calibration discrepancy between blue stars and red galaxies, described by Wright et al. (2010) and Jarrett et al. (2011). They advise a multiplicative factor of 0.92 for the *W*4 flux of all spiral and disc galaxies. As we are dealing with ETG in our sample, we have no need of such a correction. This leaves us with the third correction, which is an aperture correction due to the fact that the absolution calibration for *WISE* was done using PSF profile fitting. We apply a correction of 0.03, 0.04, 0.03 and −0.03 mag for *W*1, *W*2, *W*3 and *W*4, respectively.

We verify our measurements by comparing them with the archival and literature *WISE* fluxes, determined by flux measurements of elliptical apertures (see Fig. A3). The slopes of the data points in each of the panels are roughly parallel to the 1: 1 relation (black line). There is, however, an offset visible in all bands when comparing to the archival fluxes (blue points). Interestingly, we find systematically higher fluxes in the *W*1 and *W*4 band, while our measurements yield lower fluxes in the *W*2 and *W*3 bands.

Ciesla et al. (2014) measured the W3 and W4 fluxes of a small subset of our sample as part of the HRS (Boselli et al. 2010b). The corresponding galaxies are of the largest in our sample and include the four radio galaxies. Although the measurements were also done using aperture photometry, much more care was taken in the choice of the apertures than the automated *WISE* pipeline. Furthermore, the contribution of foreground stars is less significant in these two bands. Our agreement in both *W*3 and *W*4 with Ciesla et al. (2014) boosts confidence in our method and recommends independent flux measurements over archival *WISE* fluxes when it comes to extended sources. Our resultant fluxes for these *WISE* bands are displayed fully in Table A1.

Table A1. *WISE* photometry for the HeViCS sample. All measurements are in mJy.

VCC	F_{W1}	F_{W2}	F_{W3}	F_{W4}
94	42.8 ± 1.1	23.54 ± 0.78	22.9 ± 1.1	–
220	100.3 ± 2.6	51.6 ± 1.6	26.9 ± 1.3	13.4 ± 1.8
270	8.12 ± 0.27	3.54 ± 0.18	8.89 ± 0.49	12 ± 1.8
278	6.58 ± 0.23	3.73 ± 0.18	–	–
312	51.8 ± 1.4	26 ± 0.86	13.02 ± 0.68	–
327	4.18 ± 0.17	2.52 ± 0.14	3.77 ± 0.24	4.9 ± 1.1
345	515 ± 13	266.6 ± 7.9	110.2 ± 5.2	74.1 ± 5.7
408	233.5 ± 5.9	117.6 ± 3.5	85.8 ± 4.1	56.8 ± 4.7
411	18.61 ± 0.54	10.4 ± 0.4	–	–
450	5.3 ± 0.2	2.16 ± 0.13	8.72 ± 0.47	10.8 ± 1.6
462	64 ± 1.7	42.4 ± 1.3	29.1 ± 1.4	16 ± 2
482	13.2 ± 0.4	8.72 ± 0.34	3.67 ± 0.25	–
571	5.4 ± 0.2	2.97 ± 0.16	3.43 ± 0.23	5.7 ± 1.2
672	17.54 ± 0.51	10.6 ± 0.4	7.78 ± 0.43	10.6 ± 1.6
685	245 ± 6.2	134 ± 4	67.7 ± 3.2	34.7 ± 3.3
758	74.3 ± 1.9	39 ± 1.2	–	–
763	1417 ± 35	775 ± 23	316 ± 15	92.4 ± 6.8
781	7.29 ± 0.25	3.88 ± 0.19	2.9 ± 0.2	–
881	1902 ± 47	1026 ± 30	298 ± 14	79 ± 6
951	13.3 ± 0.4	6.06 ± 0.26	3.69 ± 0.24	–
1003	697 ± 17	370 ± 11	222 ± 10	103.9 ± 7.5
1030	311.8 ± 7.9	169.5 ± 5.1	114.1 ± 5.4	123.3 ± 8.6
1154	553 ± 14	274.5 ± 8.2	215 ± 10	130 ± 9
1226	3203 ± 80	1307 ± 38	587 ± 28	150 ± 10
1250	59 ± 1.5	33.1 ± 1.1	43.6 ± 2.1	35.4 ± 3.4
1253	430 ± 11	225.7 ± 6.7	79.4 ± 3.8	38.7 ± 3.6
1316	2275 ± 57	1067 ± 31	464 ± 22	208 ± 13
1535	854 ± 21	437 ± 13	407 ± 19	317 ± 20
1614	10.5 ± 0.33	6.82 ± 0.28	3.65 ± 0.24	1.82 ± 0.63
1619	112 ± 2.9	57.9 ± 1.8	23.3 ± 1.2	9 ± 1.5
1632	922 ± 23	451 ± 13	160.5 ± 7.6	80.2 ± 6.2
486	17 ± 0.5	10.19 ± 0.39	2.9 ± 0.2	5.6 ± 1.1
1327	56.5 ± 1.5	78.6 ± 2.4	15.53 ± 0.79	9.5 ± 1.5

This paper has been typeset from a TEX/LATEX file prepared by the author.